Direct dating of left-lateral deformation along the Red River shear zone, China and Vietnam

Lisa D. Gilley, T. Mark Harrison, P. H. Leloup, F. J. Ryerson, Oscar M. Lovera, Jiang-Hai Wang

Direct dating of left-lateral deformation along the Red River shear zone, China and Vietnam

Lisa D. Gilley,[1,2] T. Mark Harrison,[1,3] P. H. Leloup,[4] F. J. Ryerson,[5] Oscar M. Lovera,[1] and Jiang-Hai Wang[6]

Received 18 December 2001; revised 18 June 2002; accepted 20 August 2002; published 27 February 2003.

[1] Exposures of high-grade, midcrustal rocks within the Red River shear zone (RRSZ), which separates the Indochina and South China blocks, exhibit clear evidence of left-lateral, ductile deformation. Assuming that the South China Sea represents a pull-apart basin formed at the southeastern termination of the RRSZ, it has been argued that seafloor magnetic anomalies constrain the timing of sinistral slip accommodated by the RRSZ between ~32 and 17 Ma at a rate of ~4 cm/yr. While $^{40}Ar/^{39}Ar$ thermochronometry indicates that left-lateral slip occurred along the RRSZ between 25 and 17 Ma, the timing of earlier high-temperature deformation has not been directly constrained. In situ Th-Pb ion microprobe dating of monazite inclusions in garnets allows direct assessment of the timing of amphibolite-grade metamorphism and synchronous left-lateral shearing. Results from northern segments of the RRSZ in Yunnan, China, indicate that synkinematic garnet growth occurred between 34 and 21 Ma and are the first to document late Oligocene metamorphism and left-lateral shearing. Data from the southern RRSZ within Vietnam are complicated by Tertiary overprinting of rocks that experienced amphibolite facies metamorphism during the Indosinian orogeny (~220 Ma). The period during which sinistral deformation is now constrained to have occurred along the RRSZ (i.e., 34–17 Ma) is essentially coincident with spreading of the South China seafloor (32–17 Ma). This temporal and kinematic link between left-lateral shearing along the RRSZ and opening of the South China Sea supports the view that Indochina was extruded from Asia as a block along lithospheric-scale strike-slip faults. *INDEX TERMS:* 1035 Geochemistry: Geochronology; 1094 Geochemistry: Instruments and techniques; 3660 Mineralogy and Petrology: Metamorphic petrology; 8110 Tectonophysics: Continental tectonics—general (0905); 9320 Information Related to Geographic Region: Asia; *KEYWORDS:* Monazite, Th-Pb, Red River Shear Zone, garnet, in situ, South China Sea

Citation: Gilley, L. D., T. M. Harrison, P. H. Leloup, F. J. Ryerson, O. M. Lovera, and J.-H. Wang, Direct dating of left-lateral deformation along the Red River shear zone, China and Vietnam, *J. Geophys. Res.*, *108*(B2), 2127, doi:10.1029/2001JB001726, 2003.

1. Introduction

[2] The Indo-Asian collision has been accommodated by a variety of mechanisms including underthrusting of India beneath Eurasia, contractional thickening of the Eurasian lithosphere, and eastward lateral extrusion of continental blocks along lithospheric-scale strike-slip faults [*Tapponnier et al.*, 1986; *Dewey et al.*, 1989; *Houseman and England*, 1993; *Yin and Harrison*, 2000]. Knowledge of the timing and relative importance of these mechanisms is central to our understanding of how the lithosphere behaves during continent-continent collision. In particular, two models have emerged that are striking in their contrasting assumptions. One asserts that the lithosphere can be approximated as a thin viscous layer and as such shortens and thickens diffusely in response to collisional forces [e.g., *England and Houseman*, 1986]. Another view is that the lithosphere is sufficiently rigid to localize strain along lithospheric-scale shear zones and that a significant portion of Indo-Eurasian convergence was accommodated via lateral extrusion of blocks along major strike-slip faults [e.g., *Tapponnier et al.*, 1986].

[3] The Red River shear zone (RRSZ), exposed as a semicontinuous belt of gneissic massifs from northwestern Yunnan to Vietnam (Figures 1 and 2), plays a central role in the extrusion hypothesis. Much recent attention has been focused there to test model predictions, particularly the proposed link between left-lateral shearing along the RRSZ

[1]Department of Earth and Space Sciences and Institute for Geophysics and Planetary Physics, University of California, Los Angeles, California, USA.
[2]Now at Department of Geology, University of Kansas, Lawrence, Kansas, USA.
[3]Also at Research School of Earth Sciences, Australian National University, Canberra, ACT, Australia.
[4]Centre National de la Recherche Scientifique, Institut de Physique du Globe de Paris, Paris, France.
[5]Institute of Geophysics and Planetary Physics, Lawrence Livermore National. Laboratory, Livermore, California, USA.
[6]Guangzhou Institute of Geochemistry, Chinese Academy of Sciences, Guangzhou, China.

0148-0227/03/2001JB001726$09.00

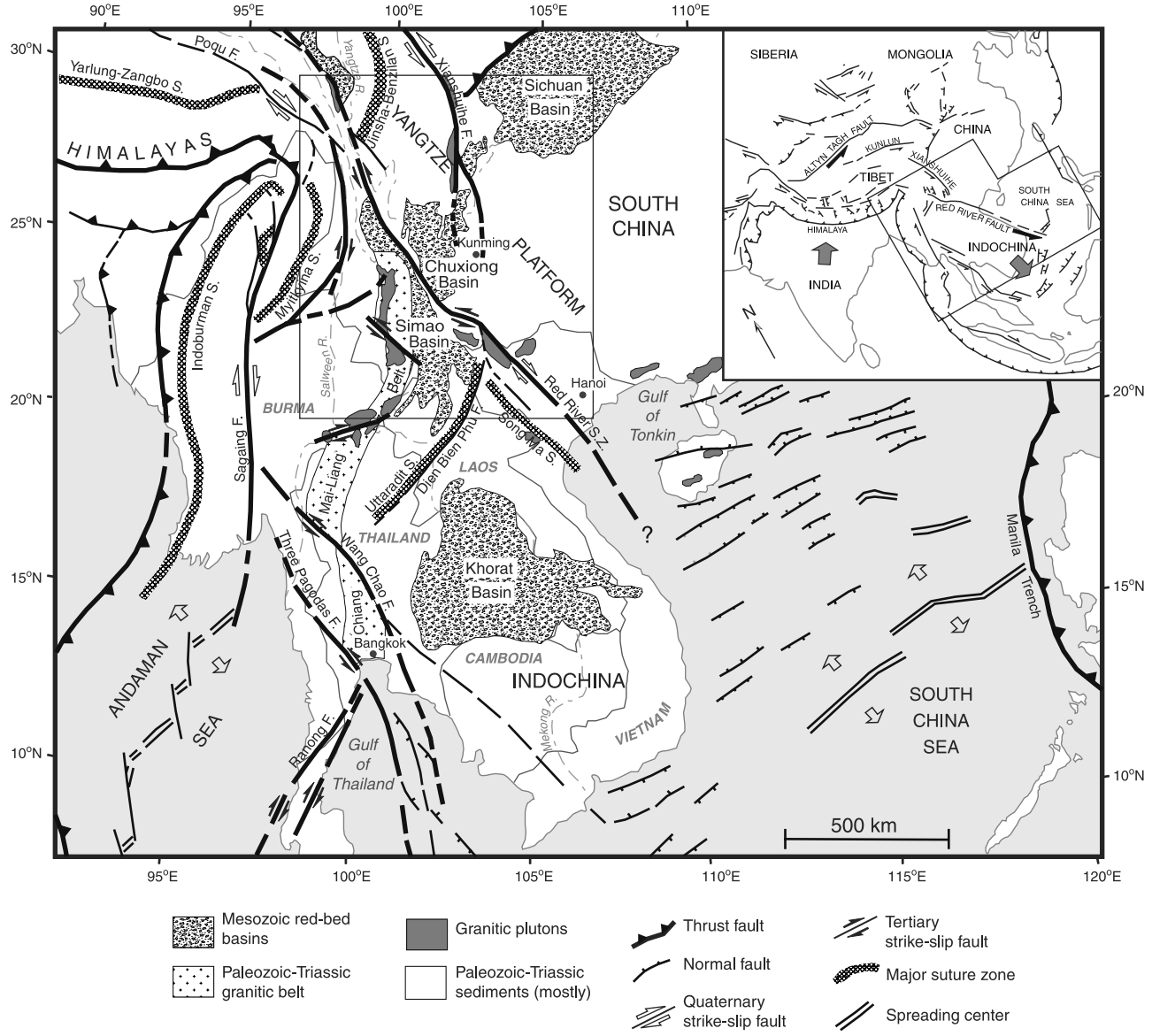

Figure 1. Geologic and tectonic map of Southeast Asia. Box indicates area of Figure 2. Inset shows the extrusion of Indochina in response to northward penetration by India. Modified after *Leloup et al.* [1995] with permission from Elsevier Science.

and seafloor spreading in the South China Sea [e.g., *Tapponnier et al.*, 1982, 1986; *Harrison et al.*, 1992, 1996; *Leloup et al.*, 1995, 2001; *Wang and Burchfiel*, 1997]. Magnetic anomalies in the South China Sea have been interpreted [*Briais et al.*, 1993] as indicating that seafloor spreading occurred between 31.5 and 16 Ma (30.5 to 17 Ma using the correlation of *Berggren et al.* [1995]) at a rate of ~4 cm/yr.

[4] Abundant geochronological evidence has been reported for late Tertiary ductile, sinistral shearing along the RRSZ [e.g., *Schärer et al.*, 1990, 1994; *Harrison et al.*, 1992, 1996; *Leloup et al.*, 1993, 2001]. U-Pb accessory mineral ages of deformed granitoids within the belt range from 26 to 22 Ma [*Schärer et al.*, 1990, 1994; *Zhang and Schärer*, 1999], indicating that high-temperature deformation occurred either during or subsequent to that period. Thermal histories derived from $^{40}Ar/^{39}Ar$ thermochronometry suggest the diachronous initiation of strike-perpendicular extension, from 25 Ma in the southeast to 17 Ma in the northwest, along a 500 km segment of the RRSZ [*Harrison et al.*, 1996]. While this relationship suggests that the onset of transtensional faulting propagated northward along the RRSZ at ~4 cm/yr, consistent with the rate of spreading of the South China seafloor [*Briais et al.*, 1993], it does not directly link rifting and seafloor spreading to sinistral slip along the RRSZ.

[5] In this paper, we report in situ Th-Pb ages of monazite inclusions in rotated garnets, which permit direct assessment of the timing of prograde metamorphism and left-lateral ductile shearing within the RRSZ. When these data are combined with thermobarometric constraints derived from selected garnet-bearing samples, pressure-temperature-time (P-T-t) paths for midcrustal gneisses of the RRSZ

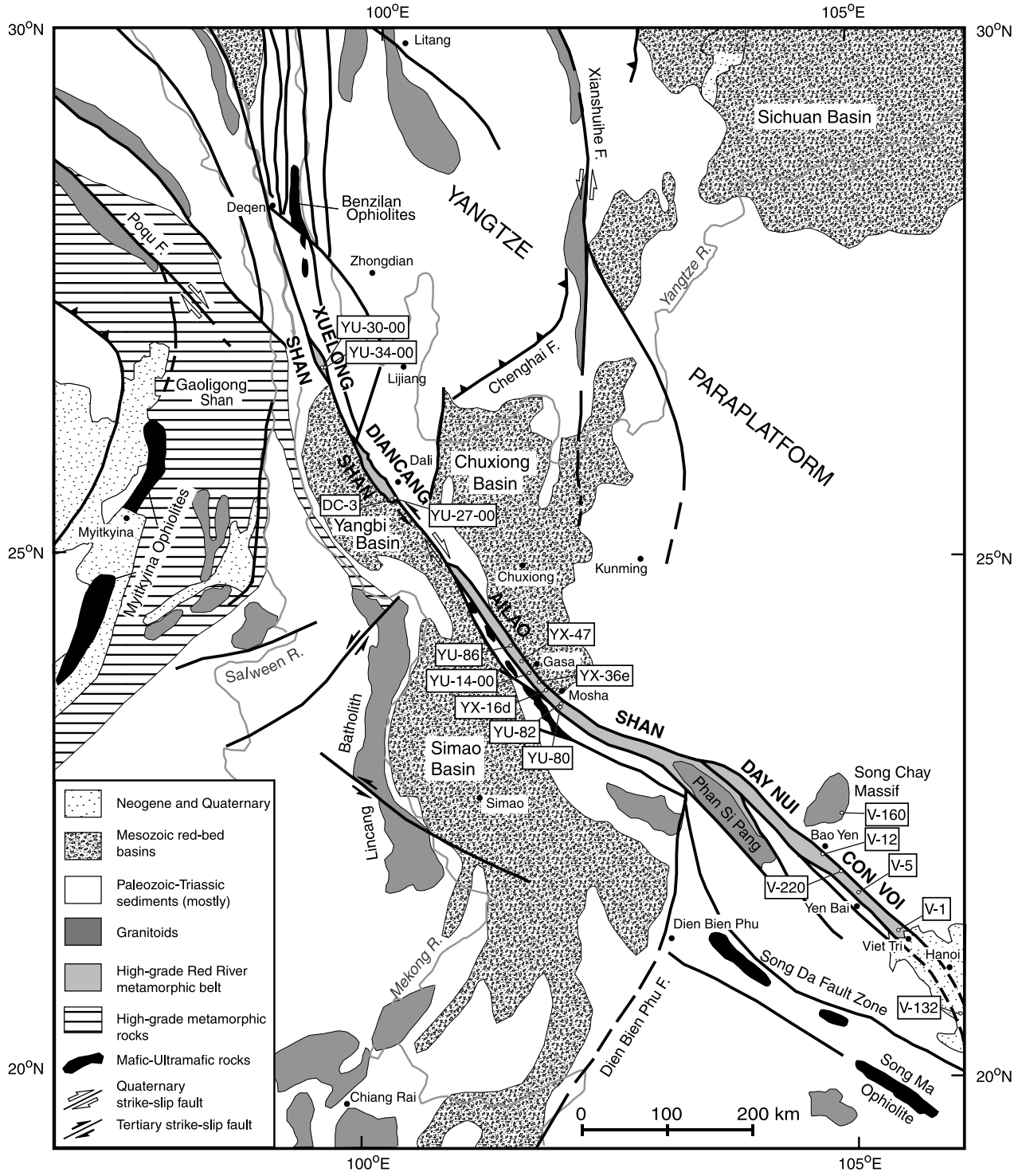

Figure 2. Geologic map of the Red River shear zone showing sample locations. See Table 1 for precise coordinates. Modified after *Leloup et al.* [1995] with permission from Elsevier Science.

can be reconstructed and used to test the viability of the extrusion hypothesis.

2. Geologic Setting of the Red River Shear Zone

[6] The RRSZ marks the boundary between the South China block to the north and the Indochina block to the south (Figures 1 and 2). Four metamorphic massifs, the Xuelong Shan, Diancang Shan, and Ailao Shan in Yunnan, China, and the Day Nui Con Voi in Vietnam, are exposed as 10–20 km wide belts of high-grade metamorphic rocks. For detailed descriptions of the geology of each range, the reader is referred to *Leloup et al.* [1995, 2001]. The cores of these four ranges consist of mylonitic gneisses and amphibolites, with less abundant migmatites, micaschists, and marbles [*Leloup et al.*, 1995].

Gneissic foliation is generally steep and roughly parallels the trend of the range, while stretching lineations are subhorizontal. A variety of kinematic indicators consistently record a left-lateral shear sense. The degree of deformation and metamorphism decreases sharply away from the metamorphic massifs. Mesozoic to Early Tertiary red bed basins on both sides of the RRSZ are gently to moderately deformed in a fashion consistent with left-lateral slip [*Tapponnier et al.*, 1986]. The presence of leucogranites within the core gneisses indicates that anatectic conditions were reached in the midcrust [*Leloup et al.*, 1999; *Wang et al.*, 2001].

[7] Extension-related exhumation of the massifs was coeval with left-lateral motion along the RRSZ [*Harrison et al.*, 1992, 1996; *Leloup et al.*, 2001]. Sinistral motion appears to have ceased at ~17 Ma, possibly due to clockwise rotation of the fault system as India impinged farther northward into Asia [*Tapponnier et al.*, 1986]. The continued deformation of Asia eventually resulted in reactivation of the RRSZ in a right-lateral sense, allowing for eastward extrusion of South China. Right-lateral transtension [*Allen et al.*, 1984; *Replumaz et al.*, 2000] along the Red River fault since ~5 Ma [*Leloup et al.*, 1993] is responsible for final exhumation of the massifs.

3. Analytical Methods

[8] Th-Pb dating of monazite was performed using a CAMECA ims 1270 ion microprobe and chemical analyses obtained using a CAMECA Camebax electron microprobe. The ion microprobe is well suited for dating of accessory minerals in rocks with polymetamorphic histories because its high spatial resolution permits dating of materials in thin section rather than on separated mineral grains, preserving textural relationships between accessory and host minerals [e.g., *Harrison et al.*, 1997]. Prior to ion microprobe analysis, textural relationships were examined in thin section using a petrographic microscope. Garnets containing accessory mineral inclusions were examined using a scanning electron microscope (SEM) and monazite was identified using backscattered electron imaging and an energy-dispersive X-ray detector. Monazites selected for ion microprobe analysis range in diameter from 20–300 μm and generally showed no compositional zonation. Portions of thin sections containing monazite and minerals used for thermobarometry were isolated using a diamond saw and mounted in epoxy along with pre-polished monazite standard blocks. Monazite grains were separated from leucogranitic samples and hand-picked onto adhesive tape along with standard grains and then mounted in 1-inch-diameter epoxy disks. After curing, mounts were polished with 0.3 μm diamond polishing compound and imaged using a SEM. Prior to ion microprobe analysis, mounts were ultrasonically cleaned and coated with ~100 Å of Au.

3.1. Th-Pb Ion Microprobe Dating

[9] Monazite ($(Ce,La,Th)PO_4$) is a valuable geochronometer due to its high concentrations of U and Th and low common Pb content. Monazite has long been used in U-Pb geochronology [e.g., *Köppel et al.*, 1980] and more recently in Th-Pb geochronology [e.g., *Harrison et al.*, 1995]. The Th-Pb system has several advantages over U-Pb dating of monazite, including high parent concentrations and rapid attainment of secular equilibrium [*Harrison et al.*, 1995]. Analytical procedures for Th-Pb dating of monazite employed in this study are described by *Harrison et al.* [1995, 1999] and briefly summarized below. A 15–25 μm diameter O^- primary beam with a current of 2 to 13 nA sputtered positive ions from the sample surface. Oxygen flooding was at times utilized to enhance the secondary ionization efficiency [*Schuhmacher et al.*, 1994]. A mass resolving power of ~5000 was sufficient to separate molecular interferences from all Pb isotopes [*Harrison et al.*, 1995]. Ion intensities of $^{204}Pb^+$, $^{207}Pb^+$, $^{208}Pb^+$, $^{232}Th^+$, ThO_2^+, and U^+ were measured using a 50 eV energy window with a 10 to 15 eV offset for $^{232}Th^+$. Pb/Th relative sensitivity factors were obtained by reference to 554 monazite (45 ± 1 Ma [*Harrison et al.*, 1999]) with a typical reproducibility of ±2%. The measured $^{208}Pb/^{204}Pb$ was corrected for common Pb assuming $^{208}Pb/^{204}Pb = 38.6$ [*Stacey and Kramers*, 1975], and ages were typically >95% radiogenic.

3.2. Interpretation of Th-Pb Monazite Ages

[10] Our monazite dating results provide clear examples of interpretive complications such as Pb loss, recrystallization, and monazite inheritance, which can be encountered in polymetamorphic terranes and result in Th-Pb monazite age distributions that are inconsistent with a single population. With these issues in mind, we characterize our results from the RRSZ gneisses in three categories.

3.2.1. Monazite Inclusions in Garnet and Matrix Monazites Yield Similar Ages

[11] In the simplest case, Th-Pb ages from monazites encompassed by prograde garnets can be interpreted as dating the timing of garnet growth, as garnet and monazite generally grow in metapelitic rocks under similar P-T conditions [*Smith and Barreiro*, 1990]. The garnet host can effectively shield a monazite inclusion from subsequent metamorphic disturbances [e.g., *Harrison et al.*, 1997; *Montel et al.*, 2000; *Catlos et al.*, 2001].

[12] Several high-grade metamorphic rocks from the RRSZ contain monazite inclusions in garnet that yield ages within error of matrix monazites (e.g., YU-14-00, YX-36e, Tables 1 and 2). We interpret these results to indicate that monazite and garnet grew simultaneously during prograde metamorphism, generally at temperatures <650°C [*Catlos et al.*, 2001]. While the experimentally determined parameters for Pb diffusion in monazite of *Smith and Giletti* [1997] suggest that rapid cooling from peak temperatures would be required for matrix monazites to quantitatively retain Pb*, the recent results of *Cherniak et al.* [2000] indicate that Pb diffusion under lithospheric conditions is negligible.

3.2.2. Monazite Inclusions in Garnet Are Older Than Matrix Monazites

[13] Samples YX-47, YX-16d, YU-86 and V-5 contain monazite inclusions that yield older ages than monazite in the rock matrix. There are several scenarios that might result in such a pattern. In garnets that experienced peak metamorphic temperatures of <650°C, monazite inclusion ages may record the timing of garnet growth, with the younger matrix monazite ages reflecting recrystallization. Another possibility is that the monazite inclusions are inherited, which would imply that the oldest matrix monazite repre-

Table 1. Sample Locations and Petrography

Sample	Site[a]	Latitude/Longitude	Rock Type	Mineralogy[b]
		Xuelong Shan		
YU-30-00	S. Weixi	27°01.3′N/99°21.4′E	garnet micaschist	qz + musc + gt + ilm + rut + ap + mon
YU-34-00	S. Weixi	27°01.3′N/99°21.5′E	garnet micaschist	qz + musc + gt + zir
		Diancang Shan		
DC-3	Xiaguan	25°33.0′N/100°8.0′E	garnet micaschist	qz + bt + musc + gt + st + plag + chl + ilm + py + ap + mon
YU-27a-00	Xiaguan	25°34.6′N/100°12.0′E	garnet micaschist	qz + musc + plag + bt + gt + chl + py + ilm + mon
YU-27b-00	Xiaguan	25°34.6′N/100°12.0′E	leucogranite vein	qz + plag + ksp + musc + bt + gt + chl + zir
		Ailao Shan		
YU-86	N. Gasa	24°13.0′N/101°22.0′E	mylonitic paragneiss	qz + plag + bt + must + ksp + sill + gt + ilm + rut + py + ap + mon + zir
YX-47	Gasa	24°05.0′N/101°31.0′E	paragneiss	qz + plag + bt + gt + ilm + py + all + mon + zir
YU-14-00	Gasa	23°59.8′N/101°32.4′E	garnet micaschist	qz + musc + plag + ksp + bt + gt + mon
YX-36e	S. Gasa	23°56.0′N/101°38.0′E	paragneiss	qz + plag + bt + gt + mon
YX-16d	N. Mosha	23°50.0′N/101°42.0′E	paragneiss	qz + plag + ksp + bt + gt + all + mon + zir
YU-80	S. Mosha	23°45.0′N/101°44.0′E	paragneiss	qz + plag + ksp + bt + gt + mon
YU-82	S. Mosha	23°45.0′N/101°45.0′E	paragneiss	qz + plag + ksp + bt + sill + gt + ilm + py + all + mon + zir
YU-4a-00	Yuanjiang	23°33.3′N/101°54.9′E	leucogranite vein	qz + plag + ksp + gt + chl + mon
YU-4c-00	Yuanjiang	23°33.3′N/101°54.9′E	leucogranite vein	qz + plag + ksp + bt + mon + zir
		Day Nui Con Voi and Song Chay Massif		
V-160	Bac Quang	22°30.0′N/104°50.0′E	garnet micaschist	qz + plag + bt + musc + gt + ilm + ap + py + all + mon + zir
V-12	Bao Yen	22°13.5′N/104°27.3′E	mylonitic micashcist	qz + ksp + plag + bt + gt + sill + mon + zir
V-220	Luc Yen	22°00.0′N/104°42.0′E	paragneiss	qz + ksp + plag + bt + gt + sill + chl + musc + ilm + py + ap + mon + zir
V-5	Yen Bai	21°47.2′N/104°54.3′E	mylonitic micashcist	qz + ksp + bt + gt + sill + ilm + ap + mon + zir
V-1	Viet Tri	21°24.3′N/105°18.7′E	mylonitic micashcist	qz + ksp + plag + bt + gt + sill + chl + cd + msc + mon + zir
V-132	Ninh Binh	20°19.8′N/106°04.5′E	mylonitic micashcist	qz + ksp + plag + bt + gt + sill + chl + musc + mon

[a]For sample locations, see Figure 2.
[b]Major minerals were identified using a petrographic microscope and scanning electron microscope. Abbreviations: qz, quartz; plag, plagioclase feldspar; ksp, K-feldspar; bt, biotite; musc, muscovite; gt, garnet; sill, sillimanite; st, staurolite; chl, chlorite; cd, chloritoid; ilm, ilmenite; rut, rutile; py, pyrite; ap, apatite; all, allanite; mon, monazite; zir, zircon.

sents an upper limit on the timing of garnet growth [e.g., *Rubatto et al.*, 2001].

[14] In rocks that experienced high-temperature metamorphism (>650°C), young matrix monazite ages could be due to diffusive loss of Pb* [*Smith and Giletti*, 1997; cf. *Cherniak et al.*, 2000]. Younger matrix monazites might reflect dissolution of preexisting monazite and new growth during a later metamorphic event that did not affect monazite inclusions due to the shielding effects of their garnet hosts [e.g., *Zhu and O'Nions*, 1999; *Montel et al.*, 2000; *Catlos et al.*, 2001].

3.2.3. Matrix and Included Monazites Yield Wide Range of Ages

[15] A more complex case arises when matrix and included monazite grains yield widely varying ages. Such a random distribution of ages is observed in rocks from the Day Nui Con Voi (e.g., V-220, V-12) that appear to have experienced very high-temperature metamorphism (section 5.3). Assuming garnet growth occurred in a single stage, there are two possible scenarios to produce this age variability: (1) growing garnet incorporated monazite of varying age, perhaps partially reset grains from a preexisting metamorphic assemblage or (2) monazites were the same age when they were incorporated by garnet but have subsequently been variably reset or recrystallized. The armoring of monazite by garnet has been documented in numerous studies [e.g., *Montel et al.*, 2000; *Foster et al.*, 2000; *Catlos et al.*, 2001], suggesting that partial resetting of monazite included in garnet is less likely than in matrix monazite.

[16] A final possibility that must be considered is that the smooth age progression observed in these samples (i.e., from Triassic to Oligocene) is due to overlapping of the primary ion beam on two or more discrete age domains. This hypothesis is consistent with the observation that multiple spots on single monazite crystals sometimes yielded very different age results (Table 2).

3.3. Thermobarometric Methods

[17] Garnet-bearing samples were selected for thermobarometric analysis based on their structural significance, mineral assemblage, and relative lack of retrograde alteration. Thin sections were examined to identify equilibrium mineral assemblages and microtextures. X-ray compositional maps of garnets (Mn, Ca, Fe, and Mg) were acquired using an EDS detector on an SEM to qualitatively evaluate garnet zoning patterns. Mineral composition data were obtained using an electron microprobe operated at 15 kV with a ~20 nA beam current. All raw data were reduced using the ZAF matrix correction [*Reed*, 1995]. Chemical zoning profiles were obtained from garnet porphyroblasts along rim-core-rim traverses at 20 to 50 μm intervals.

Table 2. Th-Pb Monazite Ion Microprobe Age Results From the RRSZ

Sample[a] Grain_Spot	Monazite ±σ, Position[b]	Age, Ma ±σ	$^{208}Pb^*$, % (±σ)	ThO_2^+/Th^+ ±σ	$^{208}Pb^+/Th^+$ × 10^{-2}±σ × 10^{-4}	$^{208}Pb^*/Th^+$,[c] × 10^{-3}±σ, × 10^{-5}
			Xuelong Shan			
YU-30-00 Calibration: (0.130 ± 0.007)x + (0.196 + 0.252); r^2 = 0.991; ThO_2^+/Th^+ = 5.658(1.622)[d]						
8_1	m	24.9 ± 0.9	68.5 ± 2.1	3.656 ± 0.021	4.804 ± 4.2	1.235 ± 4.4
9_1	m	24.6 ± 0.6	93.3 ± 0.5	3.440 ± 0.013	3.258 ± 2.3	1.216 ± 2.9
10_1	m	24.9 ± 0.6	88.9 ± 0.7	3.337 ± 0.010	3.361 ± 1.1	1.234 ± 3.2
12_1	m	18.9 ± 2.1	86.4 ± 0.9	1.686 ± 0.007	1.240 ± 0.9	0.934 ± 10.6
13_1	m	24.5 ± 0.4	96.5 ± 0.4	4.184 ± 0.046	3.855 ± 3.1	1.211 ± 2.2
13_2	m	24.1 ± 0.9	82.7 ± 1.7	3.279 ± 0.010	3.419 ± 6.8	1.191 ± 4.6
14_1	m	21.2 ± 0.8	85.5 ± 1.1	2.878 ± 0.007	2.534 ± 1.0	1.048 ± 4.2
			Diancang Shan			
DC-3 Calibration: (0.106 ± 0.009)x + (0.708 + 0.448); r^2 = 0.999; ThO_2^+/Th^+ = 6.171(0.278)[d]						
4_1	m	22.7 ± 0.5	96.5 ± 0	4.972 ± 0.019	4.71 ± 1.4	1.125 ± 2.6
YU-27a-00 Calibration: (0.105 ± 0.005)x + (0.876 + 0.119); r^2 = 0.994; ThO_2^+/Th^+ = 3.450(0.288)[d]						
1_1	m	26.5 ± 0.6	90.8 ± 0.5	2.675 ± 0.005	2.48 ± 0.6	1.313 ± 3.1
2_1	m	28.0 ± 0.9	77.2 ± 1.2	2.572 ± 0.010	2.9 ± 1.4	1.386 ± 4.3
3_1	m	25.8 ± 0.6	59.7 ± 1.1	3.116 ± 0.009	4.58 ± 2.7	1.279 ± 2.8
9_1	m	25.8 ± 0.4	85.0 ± 0.7	2.930 ± 0.010	2.94 ± 1.4	1.278 ± 2.2
11_1	m	27.0 ± 0.3	91.6 ± 0.5	3.126 ± 0.007	3.13 ± 0.8	1.336 ± 1.6
16_1	m	24.5 ± 0.4	70.6 ± 1.0	3.452 ± 0.009	4.22 ± 1.5	1.214 ± 1.9
17_1	m	27.2 ± 1.1	81.5 ± 1.1	2.309 ± 0.010	2.26 ± 1.2	1.346 ± 5.6
			Ailao Shan			
YU-86 Calibration: (0.095 ± 0.007)x + (1.120 + 0.188); r^2 = 0.995; ThO_2^+/Th^+ = 3.614(0.308)[d]						
1_1	m	21.7 ± 0.6	96.5 ± 0.6	5.481 ± 0.050	5.025 ± 8.3	1.070 ± 3.0
5_1	m	26.0 ± 0.3	96.8 ± 0.3	3.479 ± 0.006	3.298 ± 0.8	1.286 ± 1.2
6_1	m	65.6 ± 0.9	98.5 ± 0.1	3.324 ± 0.008	7.657 ± 5.4	3.252 ± 4.5
8_1	m	21.7 ± 0.7	86.5 ± 0.9	2.875 ± 0.004	2.291 ± 0.9	1.074 ± 3.7
11_1	i	34.2 ± 0.5	95.8 ± 0.4	3.283 ± 0.007	4.022 ± 1.9	1.693 ± 2.6
12_1	m	30.5 ± 0.8	92.7 ± 0.5	3.005 ± 0.007	3.227 ± 2.2	1.509 ± 4.0
15_1	m	23.0 ± 0.7	94.4 ± 0.6	2.965 ± 0.004	2.347 ± 0.9	1.141 ± 3.2
16_1	m	21.6 ± 0.3	96.1 ± 0.4	3.379 ± 0.009	2.640 ± 1.4	1.067 ± 1.5
19_1	i	31.2 ± 1.0	86.7 ± 1.3	2.925 ± 0.011	3.387 ± 1.9	1.546 ± 5.2
21_1	i	32.6 ± 1.1	89.7 ± 1.0	2.907 ± 0.010	3.379 ± 1.8	1.612 ± 5.4
YX-47 Calibration: (0.099 ± 0.010)x + (1.379 + 0.520); r^2 = 0.992; ThO_2^+/Th^+ = 7.501(1.602)[d]						
3_1	m	19.9 ± 0.4	96.1 ± 0.6	6.052 ± 0.022	4.872 ± 3.6	0.987 ± 1.8
3_2	m	22.0 ± 0.7	96.2 ± 1.2	5.425 ± 0.021	4.662 ± 3.7	1.091 ± 3.6
4_1	m	25.4 ± 2.2	98.2 ± 0.2	4.132 ± 0.007	3.582 ± 0.9	1.258 ± 11.1
8_1	i	22.3 ± 0.3	95.8 ± 1.0	8.822 ± 0.08	7.259 ± 8.6	1.100 ± 1.7
8_2	i	21.3 ± 0.7	94.8 ± 0.7	7.814 ± 0.161	7.253 ± 9.1	1.052 ± 3.4
9_1	i	31.0 ± 1.3	98.4 ± 0.2	5.083 ± 0.032	5.874 ± 6.4	1.536 ± 6.4
10_1	i	26.2 ± 0.6	76.2 ± 0.9	6.219 ± 0.056	8.360 ± 6.3	1.296 ± 2.9
11_1	m	23.5 ± 0.7	97.5 ± 0.4	5.553 ± 0.050	5.061 ± 3.7	1.164 ± 3.4
YU-14-00 Calibration: (0.120 ± 0.006)x + (0.751 + 0.165); r^2 = 0.998; ThO_2^+/Th^+ = 4.081(0.277)[d]						
1_1	m	32.2 ± 0.9	97.3 ± 0.1	2.857 ± 0.008	2.864 ± 0.7	1.600 ± 4.5
2_1	m	31.6 ± 1.5	96.1 ± 0.2	2.440 ± 0.006	2.283 ± 0.6	1.570 ± 7.5
3_2	m	33.2 ± 1.0	96.6 ± 0.1	2.812 ± 0.014	2.910 ± 0.4	1.640 ± 5.0
4_2	i	31.3 ± 0.7	97.8 ± 0.1	3.042 ± 0.012	3.010 ± 1.3	1.554 ± 3.4
5_1	m	30.0 ± 1.6	97.5 ± 0.1	2.325 ± 0.009	1.992 ± 0.5	1.492 ± 8.1
6_1	m	33.0 ± 1.5	97.1 ± 0.2	2.470 ± 0.003	2.402 ± 0.9	1.640 ± 7.5
8_1	i	33.2 ± 1.4	96.6 ± 0.2	2.525 ± 0.007	2.504 ± 0.5	1.640 ± 7.1
YX-36e Calibration: (0.128 ± 0.017)x + (0.617 + 0.781); r^2 = 0.999; ThO_2^+/Th^+ = 6.376(0.341)[d]						
1_1	m	26.7 ± 1.1	79.3 ± 1.8	5.400 ± 0.055	6.224 ± 7.7	1.322 ± 5.6
2_1	m	25.3 ± 0.6	88.9 ± 1.0	5.936 ± 0.046	5.839 ± 5.1	1.250 ± 2.8
4_1	m	24.6 ± 0.9	79.0 ± 1.3	5.636 ± 0.069	6.047 ± 7.2	1.219 ± 4.6
6_1	i	27.7 ± 0.9	95.4 ± 0.3	5.432 ± 0.033	5.410 ± 3.1	1.373 ± 4.4
7_1	m	27.3 ± 1.0	95.2 ± 0.4	5.333 ± 0.039	5.230 ± 2.5	1.353 ± 4.9
8_1	i	29.4 ± 1.1	96.0 ± 0.2	5.290 ± 0.022	5.529 ± 2.1	1.456 ± 5.3
YX-16d Calibration: (0.105 ± 0.006)x + (0.972 + 0.226); r^2 = 0.996; ThO_2^+/Th^+ = 5.297(0.361)[d]						
2_1	i	25.9 ± 0.8	85.4 ± 0.7	3.691 ± 0.011	3.877 ± 1.1	1.280 ± 4.1
3_1	i	24.1 ± 1.1	91.0 ± 0.6	3.342 ± 0.018	2.958 ± 3.1	1.195 ± 5.3
4_1	m	19.7 ± 0.4	94.6 ± 0.5	4.223 ± 0.018	3.190 ± 1.5	0.976 ± 1.8
5_1	i	23.4 ± 0.6	90.8 ± 0.6	3.957 ± 0.007	3.615 ± 1.3	1.156 ± 2.9
6_1	m	23.4 ± 0.3	96.6 ± 0.3	4.416 ± 0.012	3.850 ± 1.5	1.157 ± 1.7
7_1	m	21.1 ± 0.5	95.0 ± 0.3	4.043 ± 0.007	3.208 ± 0.8	1.043 ± 2.3
YU-80 Calibration: (0.076 ± 0.009)x + (1.824 + 0.370); r^2 = 0.999; ThO_2^+/Th^+ = 5.117(0.240)[d]						
2_1	i	29.8 ± 2.1	98.0 ± 0.2	2.997 ± 0.018	3.21 ± 1.4	1.476 ± 10.6
1_2	m	32.6 ± 1.0	98.0 ± 0.3	4.459 ± 0.021	na ± na	1.614 ± 4.7
3_1	m	24.3 ± 4.3	87.2 ± 1.1	3.103 ± 0.007	na ± na	1.205 ± 21.4
4_1	m	22.5 ± 2.0	96.4 ± 0.6	3.677 ± 0.014	na ± na	1.115 ± 9.8
5_1	m	28.4 ± 2.4	93.3 ± 0.6	3.717 ± 0.006	na ± na	1.404 ± 11.7
7_1	m	23.1 ± 0.6	92.1 ± 0.7	4.563 ± 0.010	na ± na	1.142 ± 2.9

Table 2. (continued)

Sample[a] Grain_Spot	Monazite ±σ, Position[b]	Age, Ma ±σ	$^{208}Pb^*$, % (±σ)	ThO_2^+/Th^+ ±σ	$^{208}Pb^+/Th^+$ × 10^{-2}±σ × 10^{-4}	$^{208}Pb^*/Th^+$,[c] × 10^{-3}±σ, × 10^{-5}
YU-82 Calibration: (0.109 ± 0.011)x + (0.695 + 0.542); r^2 = 0.999; ThO_2^+/Th^+ = 6.180(0.156)[d]						
1_1	m	27.1 ± 0.9	73.1 ± 0.9	5.222 ± 0.020	7.610 ± 17.5	1.344 ± 4.3
3_1	m	25.0 ± 5.4	86.4 ± 1.2	2.419 ± 0.037	2.254 ± 3.6	1.235 ± 26.9
4_1	m	29.3 ± 0.7	92.6 ± 0.5	5.201 ± 0.038	6.450 ± 2.8	1.449 ± 3.5
5_1	m	74.1 ± 2.5	99.1 ± 0.1	4.843 ± 0.018	14.06 ± 2.1	3.673 ± 12.3
Calibration: (0.139 ± 0.020)x + (−0.593 + 0.777); r^2 = 0.999; ThO_2^+/Th^+ = 4.741(0.128)[d]						
7_1	m	20.6 ± 0.2	91.4 ± 0.3	4.370 ± 0.006	3.975 ± 1.4	1.021 ± 1.2
8_1	m	52.9 ± 1.1	94.1 ± 0.3	4.095 ± 0.010	9.350 ± 1.9	2.618 ± 5.3
10_1	m	23.9 ± 0.8	92.0 ± 0.4	3.784 ± 0.015	4.030 ± 1.4	1.181 ± 3.8
12_1	m	23.1 ± 0.3	95.9 ± 0.3	4.255 ± 0.011	4.148 ± 1.3	1.144 ± 1.7
15_1	m	27.8 ± 0.5	97.3 ± 0.2	4.115 ± 0.008	4.771 ± 1.1	1.375 ± 2.7
16_1	m	26.5 ± 0.7	97.6 ± 0.2	3.893 ± 0.010	4.319 ± 0.9	1.310 ± 3.6
18_1	m	34.3 ± 0.6	96.1 ± 0.2	4.249 ± 0.006	6.140 ± 4.0	1.699 ± 2.7
YU-4a-00 Calibration: (0.225 ± 0.038)x + (−5.367 + 1.864); r^2 = 0.999; ThO_2^+/Th^+ = 5.875(0.442)[d]						
2_1	r	21.4 ± 0.4	97.5 ± 0.2	4.586 ± 0.016	4.800 ± 2.1	1.060 ± 2.1
2_2	c	21.1 ± 0.5	97.7 ± 0.2	4.491 ± 0.015	4.672 ± 1.5	1.044 ± 2.3
6_1	c	21.8 ± 0.4	97.3 ± 0.2	4.658 ± 0.018	4.930 ± 2.5	1.078 ± 2.1
7_1	r	21.9 ± 0.4	98.0 ± 0.2	4.849 ± 0.025	5.010 ± 3.1	1.083 ± 1.8
8_1	c	21.5 ± 0.4	97.0 ± 0.2	4.687 ± 0.018	4.891 ± 2.2	1.063 ± 2.0
9_1	c	22.0 ± 0.3	97.8 ± 0.2	4.851 ± 0.031	5.046 ± 2.0	1.088 ± 1.7
YU-4c-00 Calibration: (0.225 ± 0.038)x + (−5.367 + 1.864); r^2 = 0.999; ThO_2^+/Th^+ = 5.875(0.442)[d]						
1_1	c	10.1 ± 1.1	99.1 ± 0.4	1.495 ± 0.009	1.535 ± 1.3	0.500 ± 5.2
1_2	c	9.8 ± 1.0	98.8 ± 0.6	1.482 ± 0.011	1.493 ± 1.3	0.486 ± 5.1
Day Nui Con Voi and Song Chay Massif						
V-160 Calibration: (0.098 ± 0.006)x + (0.905 + 0.151); r^2 = 0.999; ThO_2^+/Th^+ = 3.347(0.154)[d]						
1_1	m	246.3 ± 8.1	99.1 ± 0.1	2.533 ± 0.007	20.5 ± 14	12.26 ± 40
2_1	i	216.4 ± 39.2	96.0 ± 0.2	1.525 ± 0.003	7.08 ± 3.6	10.76 ± 196
3_1	m	224.1 ± 7.2	99.4 ± 0.0	2.525 ± 0.009	18.5 ± 10	11.15 ± 36
4_1	m	254.8 ± 14.4	99.1 ± 0.1	2.185 ± 0.004	16.7 ± 6	12.69 ± 72
5_1	m	229.7 ± 4.7	99.7 ± 0.0	2.762 ± 0.003	21.7 ± 6	11.43 ± 23
7_1	m	202.9 ± 4.6	91.3 ± 0.3	2.739 ± 0.006	20.7 ± 10	10.09 ± 23
8_1	i	379.8 ± 16.7	99.8 ± 0.0	2.343 ± 0.008	27.8 ± 16	18.97 ± 84
9_1	i	419.3 ± 3.0	99.8 ± 0.0	3.162 ± 0.004	48.3 ± 18	20.96 ± 15
10_1	m	240.4 ± 3.3	99.7 ± 0.0	2.935 ± 0.006	24.8 ± 10	11.97 ± 17
V-220 Calibration: (0.243 ± 0.015)x + (−2.395 + 0.579); r^2 = 0.999; ThO_2^+/Th^+ = 6.767(0.183)[d]						
1_1	m	29.5 ± 0.3	93.3 ± 0.4	7.792 ± 0.025	6.57 ± 1.7	1.460 ± 1.3
2_1	i	121.5 ± 1.7	99.1 ± 0.0	7.440 ± 0.028	24.6 ± 33	6.030 ± 8.6
3_1	i	187.6 ± 1.0	99.5 ± 0.0	7.303 ± 0.035	37.4 ± 17	9.324 ± 5.1
4_1	i	210.2 ± 0.7	99.4 ± 0.0	7.016 ± 0.014	40.8 ± 9	10.45 ± 3.5
5_1	i	202.6 ± 0.6	99.4 ± 0.0	6.777 ± 0.024	38.3 ± 11	10.07 ± 3.2
6_1	i	50.0 ± 0.2	98.8 ± 0.1	7.292 ± 0.023	9.99 ± 2.9	2.474 ± 1.2
6_2	i	170.7 ± 0.8	99.5 ± 0.0	6.430 ± 0.024	31 ± 8	8.479 ± 4.1
6_3	i	44.6 ± 0.3	98.9 ± 0.1	7.501 ± 0.025	9.1 ± 2.5	2.209 ± 1.4
7_1	m	61.9 ± 0.5	97.7 ± 0.1	6.923 ± 0.020	12.1 ± 8	3.067 ± 2.5
9_1	m	31.5 ± 0.1	98.0 ± 0.1	6.896 ± 0.023	6.09 ± 1.1	1.561 ± 0.5
9_2	m	176.5 ± 0.6	99.5 ± 0.0	6.652 ± 0.015	32.80 ± 10	8.768 ± 3.1
V-12 Calibration: (0.062 ± 0.008)x + (1.871 + 0.208); r^2 = 0.996; ThO_2^+/Th^+ = 3.617(0.204)[d]						
2_1	i	117.1 ± 1.8	98.8 ± 0.2	3.695 ± 0.010	17.40 ± 8	5.808 ± 8.8
5_1	m	168.0 ± 5.6	98.9 ± 0.1	3.215 ± 0.005	18.4 ± 3	8.346 ± 27.9
6_1	m	27.5 ± 0.3	97.0 ± 0.3	3.620 ± 0.006	3.99 ± 0.8	1.363 ± 1.7
7_1	m	127.9 ± 1.9	98.9 ± 0.1	3.433 ± 0.006	16.3 ± 6	6.348 ± 9.7
8_1	i	85.1 ± 1.1	98.8 ± 0.1	3.498 ± 0.004	11.3 ± 2	4.218 ± 5.3
9_1	m	81.2 ± 3.2	95.4 ± 0.2	3.168 ± 0.008	8.880 ± 2.3	4.026 ± 15.8
V-5 Calibration: (0.097 ± 0.020)x + (1.477 + 0.872); r^2 = 0.996; ThO_2^+/Th^+ = 8.504(2.024)[d]						
1_1	m	29.4 ± 1.0	96.4 ± 0.4	6.543 ± 0.032	7.9 ± 3.8	1.454 ± 5.1
2_1	m	25.1 ± 0.9	89.4 ± 2.5	5.632 ± 0.074	5.97 ± 7.5	1.242 ± 4.4
3_1	m	28.4 ± 2.0	96.5 ± 0.4	4.729 ± 0.027	4.9 ± 4.5	1.407 ± 9.7
5_1	m	41.6 ± 1.3	96.3 ± 0.3	5.322 ± 0.014	8.5 ± 4.4	2.058 ± 6.3
6_1	i	52.1 ± 3.2	98.8 ± 0.2	4.815 ± 0.022	9 ± 7.0	2.579 ± 16.0
7_1	i	168.6 ± 3.2	99.1 ± 0.1	5.641 ± 0.026	36.40 ± 17	8.376 ± 15.9
8_1	i	66.3 ± 2.4	95.5 ± 0.5	6.605 ± 0.038	18.2 ± 11	3.283 ± 12.1
9_1	m	23.0 ± 2.4	56.0 ± 5.7	5.661 ± 0.063	8.79 ± 12	1.138 ± 11.9
11_1	i	64.3 ± 1.7	92.1 ± 0.7	6.203 ± 0.030	16.9 ± 14	3.186 ± 8.4
12_1	i	43.5 ± 0.9	96.4 ± 0.3	5.590 ± 0.024	9.51 ± 7.6	2.155 ± 4.4
13_1	i	48.9 ± 0.9	96.5 ± 0.3	5.791 ± 0.013	11.20 ± 5	2.422 ± 4.3
14_1	i	75.3 ± 5.6	93.2 ± 1.8	8.019 ± 0.094	27.1 ± 36	3.732 ± 27.8
V-1[e] Calibration: (0.114 ± 0.017)x + (0.488 + 0.402); r^2 = 0.998; ThO_2^+/Th^+ = 3.204(0.177)[d]						
1_1	m	102.5 ± 3.3	98.7 ± 0.1	2.749 ± 0.017	10.3 ± 4	5.085 ± 16.6
2_1	m	21.3 ± 1.3	95.6 ± 0.3	2.409 ± 0.013	1.86 ± 1.4	1.054 ± 6.6
3_1	m	208.0 ± 3.5	98.2 ± 0.0	2.966 ± 0.007	23 ± 10	10.34 ± 18
5_1	i	210.2 ± 9.8	99.4 ± 0.0	2.565 ± 0.011	19.2 ± 17	10.45 ± 49

Table 2. (continued)

Sample[a] Grain_Spot	Monazite ±σ, Position[b]	Age, Ma ±σ	^{208}Pb*, % (±σ)	ThO_2^+/Th^+ ±σ	$^{208}Pb^+/Th^+$ × 10^{-2}±σ × 10^{-4}	^{208}Pb*/Th^+,[c] × 10^{-3}±σ, × 10^{-5}
7_1	m	152.5 ± 3.6	99.0 ± 0.1	2.859 ± 0.019	16 ± 14	7.574 ± 17.9
9_1	m	27.0 ± 0.7	95.0 ± 0.2	2.851 ± 0.014	2.93 ± 2.1	1.336 ± 3.2
10_1	m	52.8 ± 1.2	78.3 ± 0.6	2.913 ± 0.010	7.14 ± 4.2	2.617 ± 5.8
11_1 *e*	m	26.0 ± 0.4	90.2 ± 0.4	2.997 ± 0.017	3.16 ± 2.4	1.289 ± 2.1
11_2 *e*	m	31.2 ± 0.6	92.9 ± 0.3	3.230 ± 0.020	4.02 ± 9.3	1.547 ± 3.0
11_3 *e*	m	39.7 ± 0.9	95.1 ± 0.3	3.509 ± 0.017	5.5 ± 10.2	1.966 ± 4.4
12_1	i	220.0 ± 5.8	99.6 ± 0.0	2.816 ± 0.011	22.5 ± 9	10.94 ± 29
13_1	i	224.1 ± 6.0	99.6 ± 0.0	2.813 ± 0.012	22.90 ± 18	11.15 ± 30
18_1	m	24.6 ± 0.8	95.2 ± 0.3	2.750 ± 0.010	2.54 ± 0.9	1.216 ± 3.8
21_1	i	211.8 ± 7.4	98.7 ± 0.1	2.716 ± 0.030	20.9 ± 22	10.53 ± 37
22_1 *e*	m	44.1 ± 4.4	95.8 ± 0.3	2.201 ± 0.031	3.44 ± 21	2.185 ± 21.6
22_2 *e*	m	79.8 ± 5.1	97.8 ± 0.1	2.682 ± 0.019	7.81 ± 46	3.954 ± 25.1
22_3 *e*	m	131.9 ± 4.3	99.0 ± 0.1	2.811 ± 0.010	13.5 ± 26	6.549 ± 21.3
23_1	i	222.0 ± 3.7	99.3 ± 0.0	3.006 ± 0.016	24.6 ± 21	11.05 ± 19
V-132 Calibration: (0.115 ± 0.006)x + (0.568 + 0.326); r^2 = 0.986; ThO_2^+/Th^+ = 7.280(0.070)[d]						
2_1	m	32.2 ± 0.6	97.7 ± 0.3	5.984 ± 0.094	7.691 ± 6.5	1.592 ± 3.0
5_1	m	43.1 ± 0.8	96.1 ± 0.3	5.815 ± 0.072	10.16 ± 5	2.136 ± 4.1
9_1	m	50.3 ± 1.1	95.1 ± 0.4	5.281 ± 0.037	10.76 ± 6	2.492 ± 5.4
10_1	m	73.6 ± 1.6	98.7 ± 0.1	5.371 ± 0.045	15.47 ± 9	3.648 ± 8.0
11_1	m	46.7 ± 0.9	98.3 ± 0.2	5.533 ± 0.039	10.18 ± 6	2.313 ± 4.3
12_1	m	107.1 ± 1.3	97.3 ± 0.2	7.415 ± 0.049	32.57 ± 2	5.312 ± 6.3
13_1	m	44.9 ± 1.0	97.2 ± 0.2	5.526 ± 0.059	9.883 ± 7.7	2.225 ± 4.9

[a]Nomenclature indicates the grain and spot number, respectively, of each analyzed monazite See Figure 2 for sample locations.
[b]Textural position of monazite grain; m, matrix; i, inclusion in garnet. For monazites measured on grain mounts, position indicates location of ion probe spot; r, rim; c, core.
[c]Measured ratio corrected for common Pb assuming $^{208}Pb/^{204}Pb$ = 38.6.
[d]Th calibration line: (slope ± 1σ)x + (intercept ± 1σ); r^2 is correlation; ThO_2^+/Th^+ = average (SD).
[e]Analyses 1, 2, and 3 of monazites 11 and 22 from sample V-1 were measured on the same spot. Both percent ^{208}Pb* and Th-Pb age increase as the ion beam drills deeper into the grain.

Compositions of biotite, muscovite, chlorite, plagioclase, and ilmenite were measured using multiple spot analyses to assess variability within individual grains. Sillimanite, rutile, and quartz were treated as pure phases.

[18] Calculation of peak metamorphic P-T conditions for samples from the RRSZ using garnet thermobarometry is complicated by diffusional relaxation of original garnet zoning, retrograde ion exchange, and retrograde transfer reactions. Multiple thermometers and barometers were utilized to assess internal consistency and several solution models were used to minimize uncertainties resulting from individual calibrations. Equilibria were calculated using the software Thermobarometry v1.9 [*Spear and Kohn*, 1995].

4. Geochronologic Results

[19] Th-Pb ages were obtained for 18 monazite samples from the RRSZ (Table 2). Sample locations are given in Table 1 and are shown in Figure 2. BSE images of representative dated monazite grains are shown in Figure 3. Individual age uncertainties are quoted at the ±1σ level and weighted mean ages at the ±2σ level.

[20] Zircons from six RRSZ samples were analyzed in situ and in grain mounts using the ion microprobe [see *Gilley*, 2001]. However, with the exception of sample YU-4c-00 (section 4.3), these samples do not record evidence of Tertiary metamorphism. Concordant U-Pb ages range from Precambrian to Early Triassic, which we interpret to reflect protolith ages.

4.1. Geochronology of the Xuelong Shan: South Weixi Section

[21] Sample YU-30-00 is a micaschist from the southern Xuelong Shan. Garnet porphyroblasts are large (>1 cm), have skeletal rims, and are dissected by an extensive latticework of Fe-oxide and pyrite. This high degree of secondary alteration renders garnets unsuitable for thermobarometry. Asymmetric tails on garnet porphyroblasts provide evidence for high temperature left-lateral deformation. Ion microprobe analysis of matrix monazites yielded Th-Pb ages between ~25 and 19 Ma (Figure 3a). We interpret this 6 m.y. age range to reflect continued monazite growth during an extended episode of metamorphism and sinistral shearing rather than Pb loss [*Cherniak et al.*, 2000].

4.2. Geochronology of the Diancang Shan: Xiaguan Section

[22] Monazite from two pelitic schists, YU-27a-00 and DC-3, were dated in situ. Sample DC-3 contains large porphyroblasts of garnet and staurolite in a fine-grained matrix. Pyrite grew in garnet pressure shadows following left lateral deformation. No monazite or zircon inclusions could be located in DC-3 garnets, but a matrix monazite yielded a Th-Pb age of 22.7 ± 0.5 Ma. Sample YU-27a-00 contains a relatively homogenous population of monazite. Seven matrix monazites ranging from 20 to 60 μm in diameter yielded a weighted mean age of 26.1 ± 0.3 Ma (mean square of weighted deviation (MSWD) = 5.2).

[23] Th-Pb ages recorded by monazite from DC-3 and YU-27a-00 (i.e., 28–22 Ma) are similar to previously documented U-Pb ages from anatectic leucogranites, which document high-temperature left-lateral deformation in the Diancang Shan at or subsequent to 25–22 Ma [*Schärer et al.*, 1990, 1994]. *Schärer et al.* [1994] reported an age of 35 Ma for an undeformed monzonitic intrusion ~50 km outside of the shear zone, and suggested that this age dates early stages of left-lateral ductile deformation along the RRSZ. Although this age provides evidence for elevated temper-

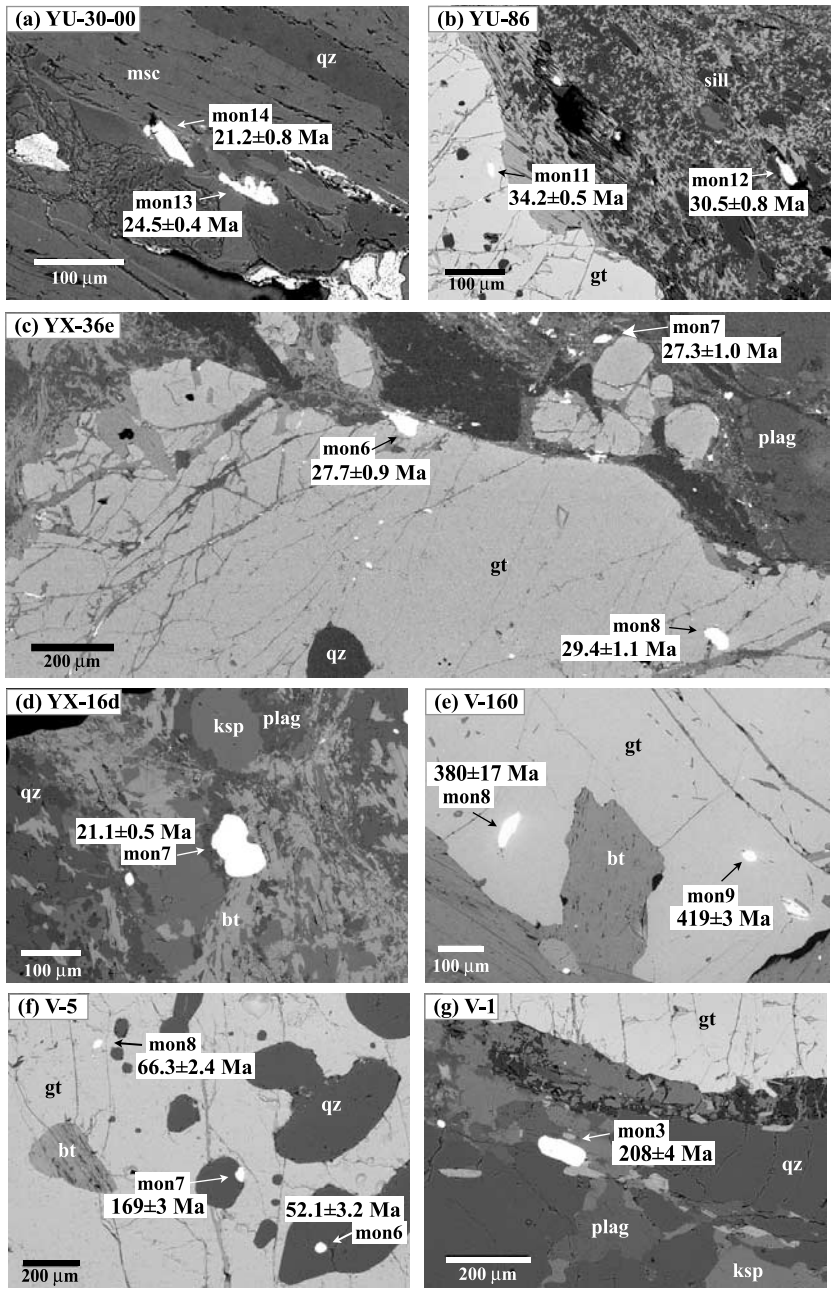

Figure 3. Backscattered electron images of representative monazite grains dated from the Xuelong Shan (YU-30-00), Ailao Shan (YU-86, YX-36e, YX-16d), Song Chay massif (V-160), and Day Nui Con Voi (V-1, V-5) showing Th-Pb ages (±1σ). See Table 2 for details of the age data. Abbreviations are mon, monazite; gt, garnet; bt, biotite; plag, plagioclase; sill, sillimanite; ksp, K-feldspar; msc, muscovite; qz, quartz.

atures in the lower crust in the late Eocene, it does not directly constrain the timing of shearing along the RRSZ.

4.3. Geochronology of the Ailao Shan

4.3.1. North Gasa Section

[24] Sample YU-86, collected from the eastern Ailao Shan (Figure 2), is a garnet-bearing mylonitic paragneiss. Stretched garnet porphyroblasts contain inclusions of quartz, biotite, plagioclase, rutile, monazite, and zircon. Quartz and biotite inclusions are generally concentrated in garnet cores, which are surrounded by ~200 μm thick, inclusion-free rims. Quartz inclusions in garnets show no subgrain boundaries or undulose extinction, suggesting static annealing at elevated temperatures. Sillimanite shear bands and synkinematic garnets provide clear evidence for high temperatures left-lateral ductile deformation. Porphyroblasts of K-feldspar produced from the dehydration of muscovite at high temperatures are commonly surrounded by a mantle of plagioclase. Matrix biotite is fine-grained and intimately associated with muscovite, suggesting retrograde

growth of biotite and muscovite as a result of garnet dissolution and breakdown of K-feldspar and sillimanite.

[25] Monazite inclusions in a single garnet yielded Th-Pb ages of 32.6 ± 1.1 Ma and 31.2 ± 1.0 Ma. An inclusion from near the rim of a second garnet was dated at 34.2 ± 0.5 Ma (Figure 3b). Three of the seven matrix monazites yielded a weighted mean age of 21.6 ± 0.3 Ma (MSWD = 1.9; n = 6), significantly younger than the monazite inclusion ages. The remaining matrix monazites yielded ages between 31 and 23 Ma, with the exception of one 66 Ma age which we interpret to represent incomplete recrystallization of preexisting monazite during Oligocene metamorphism. These results extend the range of monazite ages previously obtained from deformed leucogranites in the Ailao Shan, which were interpreted to record magmatism between 25 and 22 Ma [*Schärer et al.*, 1990, 1994].

4.3.2. Gasa Section

[26] Monazite inclusions in three garnets from sample YX-47, a garnet-bearing paragneiss, yielded ages of 31.0 ± 1.3, 26.2 ± 0.6, and 21.3 ± 0.7 Ma. Matrix monazites were dated between 25 and 20 Ma. YU-14-00 is a garnet-bearing metapelitic schist and contains garnets that are typically small (<300 μm) in the plane of the foliation. A monazite inclusion in garnet yielded an age of 33.2 ± 1.4 Ma. Six matrix monazite grains cluster between 33 and 30 Ma, giving a weighted mean age of 31.8 ± 0.6 Ma (MSWD = 0.8).

4.3.3. South Gasa Section

[27] Two monazite inclusions in a single garnet from YX-36e, a garnet-bearing paragneiss, yielded Th-Pb ages of 29.4 ± 1.1 Ma and 27.7 ± 0.9 Ma (Figure 3c). Four matrix monazites yielded a somewhat younger age range of 27 to 25 Ma, giving a weighted mean age of 25.7 ± 0.6 Ma (MSWD = 1.8). We interpret the slightly younger ages of the matrix monazites to indicate minor Pb loss and/or recrystallization during retrograde cooling.

4.3.4. North Mosha Section

[28] Sample YX-16d is a garnet gneiss containing abundant monazite and zircon, both in the matrix and as inclusions in garnet. Allanite occurs rarely in rims around monazite crystals. Three monazite inclusions in a single garnet were dated at 25.9 ± 0.8 Ma, 24.1 ± 1.1 Ma, and 23.4 ± 0.6 Ma. Matrix monazites yielded slightly younger ages of 23.4 ± 0.3 Ma, 21.1 ± 0.5 Ma (Figure 3d), and 19.7 ± 0.4 Ma.

4.3.5. South Mosha Section

[29] Monazites from two garnet-bearing paragneiss samples, YU-80 and YU-82, were collected from south of Mosha. A single monazite inclusion in garnet from YU-80 was dated at 29.8 ± 2.1 Ma. Matrix monazites yielded ages between ~32 and 22 Ma. The younger ages may be due to diffusive Pb loss or continued crystallization of monazite.

[30] Sample YU-82 did not contain monazite inclusions. Nine of the eleven matrix monazites analyzed yielded ages between 34 and 21 Ma. Two grains yielded ages of 74.1 ± 2.5 and 52.9 ± 1 Ma, indicating the presence of incompletely reset detrital monazite. These data suggest that thermal conditions experienced during Tertiary metamorphism were not alone sufficient to reset Th-Pb ages of monazite and thus the 34–21 Ma ages record the timing of monazite crystallization.

4.3.6. Yuanjiang Section

[31] Samples YU-4a-00 and YU-4b-00 are leucogranite veins collected from a river-polished outcrop of gneiss near Yuanjiang. The gneissic foliation contains numerous boudin trails deformed in a left-lateral sense. YU-4a-00 was observed to be the least deformed, and therefore most recent, vein crosscutting the foliation of the host gneiss. YU-4c-00 appears to be cut by YU-4a-00 and is oriented parallel to the foliation in the host gneiss. Monazite and zircon, present in low abundances in these leucogranites, were separated and analyzed in grain mounts.

[32] Th-Pb analysis of six separated monazite grains from YU-4a-00 yielded a weighted mean age of 21.7 ± 0.2 Ma (MSWD = 0.6). Since YU-4a-00 cuts the foliation of the host gneiss, the gneissic foliation must have developed prior to 22 Ma. Curiously, two spots on one monazite grain from YU-4c-00 yielded Th-Pb ages of 10.1 ± 1.1 and 9.9 ± 1.0 Ma. This ~10 Ma age appears inconsistent with the structural relationship between the two veins and the age of the gneissic foliation (>22 Ma) and we assume it is due to late recrystallization in the presence of a low pH aqueous fluid [e.g., *Townsend et al.*, 2000]. U-Pb zircon ages from YU-4c-00 are consistent with an intrusion age of ~30 Ma coupled with older inherited components (~200 and ~575 Ma) [*Gilley*, 2001].

4.4. Geochronology of the Song Chay Dome

[33] A single micaschist (V-160) was analyzed from the Song Chay massif (Figure 2) in order to elucidate the thermal history experienced by rocks outside of the shear zone. Garnets in V-160 commonly contain inclusions of quartz and biotite. Monazite inclusions in a single garnet yielded Th-Pb ages of 419 ± 3 and 380 ± 17 Ma (Figure 3e). Another monazite inclusion, located on a crack near the margin of a fragmented garnet, was dated at 216 ± 39 Ma. Six matrix monazites yielded ages between 255 and 203 Ma, significantly younger than the inclusion ages. Two zircon inclusions and three matrix zircons yielded a concordant U-Pb age of ~419 Ma, identical to the oldest age of monazite included in garnet [*Gilley*, 2001]. The age range exhibited by matrix monazites (255–203 Ma) indicates either partial resetting of older crystals or growth of new monazite during a Triassic metamorphic event, probably the Indosinian orogeny that affected the Song Chay dome [*Roger et al.*, 2000; *Maluski et al.*, 2001]. Monazite inclusions preserve older ages corresponding to granite crystallization in the Song Chay massif at 428 ± 5 Ma [*Roger et al.*, 2000].

4.5. Geochronology of the Day Nui Con Voi

4.5.1. Bao Yen Section

[34] Sample V-12 is a mylonitic garnet-gneiss from the northeastern margin of the Day Nui Con Voi. Garnet porphyroblasts contain inclusions of plagioclase and biotite in addition to rare inclusions of monazite and zircon. Shear planes and asymmetric tails on garnet porphyroblasts provide evidence for left-lateral ductile deformation. Two monazite inclusions (both located on cracks in garnet) yielded Th-Pb ages of 117 ± 2 and 85.1 ± 1.1 Ma. Matrix monazites gave a broad range of ages: 168 ± 6, 128 ± 2, 81.2 ± 3.2, and 27.5 ± 0.3 Ma. We interpret this age range to reflect partial resetting of a preexisting (perhaps Indosinian) metamorphic assemblage during Oligocene deformation along the RRSZ.

4.5.2. Luc Yen Section

[35] Eleven monazite analyses from V-220, a garnet-bearing gneiss, produced ages that range from Late Triassic

to late Oligocene, similar to the age range obtained from V-12. Multiple spots on single grains yielded very different ages (e.g., 177 and 31 Ma for a monazite in the matrix; 171, 50, and 45 Ma for an inclusion near a garnet rim), suggesting that this rock has experienced multiple metamorphic and/or deformational episodes. The age range of inclusions (210 to 122 Ma and 50 to 45 Ma) suggests multiple phases of garnet growth. Garnet cores contain monazites that yield Mesozoic ages, whereas Tertiary monazites were observed only within garnet rims. These age patterns point to an early phase of garnet growth in the Late Triassic to Cretaceous, followed by a second phase in the Eocene.

4.5.3. Yen Bai Section

[36] Sample V-5 is a garnet-bearing mylonitic micaschist. Garnet porphyroblasts are large (>4 mm), elongated parallel to the stretching lineation, and contain inclusions of quartz, biotite, sillimanite, ilmenite, rutile, monazite and zircon. The mineral assemblage is suggestive of high-temperature metamorphism above the second sillimanite isograd. Biotite shear bands and asymmetric pressure shadows on garnets provide evidence for top-to-the-north ductile deformation compatible with left-lateral shear on the RRSZ [*Leloup et al.*, 2001]. Garnet cores are rich in inclusions and are surrounded by thick, nearly inclusion-free rims. Quartz inclusions are aligned along their c-axes and oriented oblique to the matrix foliation, suggestive of differential rotation of garnet porphyroblasts. Brittle fractures in garnet and sillimanite perpendicular to the foliation indicate late-stage stretching.

[37] Four monazite inclusions in an elongated garnet yielded ages (in order of increasing distance from the garnet rim) of 41.6 ± 1.3, 66.3 ± 2.4, 52.1 ± 3.2, and 169 ± 3 Ma (Figure 3f). The ~42 Ma monazite probably has not benefited from the shielding effects of garnet because it is only partially included. Three monazites from a second garnet were dated (in order of increasing distance from the rim) at 48.9 ± 0.9 Ma, 43.5 ± 0.9 Ma, and 75.3 ± 5.6 Ma. A seventh monazite inclusion was dated at 64.3 ± 1.7 Ma. Matrix monazites yielded younger ages, clustering between 29 and 23 Ma.

[38] The apparent progression of monazite inclusion ages from garnet cores to rims could indicate multiple episodes of garnet growth. Because all original compositional zonation in garnets from V-5 has been erased (see section 5.3), these episodes would not be evident from the chemical data. However, such an extended period for garnet growth seems unlikely, particularly in view of the fact that this age pattern was not observed in any of the other Day Nui Con Voi samples. Rather, we suggest that garnet growth in V-5 occurred in a single stage, post-dating the age of the youngest monazite inclusion (~44 Ma). Monazite inclusions dated between 170 and 43 Ma are inherited or represent differential resetting of a preexisting metamorphic assemblage via diffusional Pb loss or recrystallization during or prior to garnet growth. Given that matrix monazites are generally larger in size than included monazites, we interpret the 29 to 23 Ma matrix monazites ages to indicate matrix monazite growth during Oligocene metamorphism. However, the data do not preclude the possibility that garnet growth occurred much earlier, and that monazite inclusions were reset subsequent to incorporation by garnet.

4.5.4. Viet Tri Section

[39] V-1, a mylonitic garnet-micaschist, contains garnet porphyroblasts that are elongated parallel to the stretching lineation and contain inclusions of sillimanite, quartz, biotite, monazite and zircon and. Biotite, muscovite, and chlorite are common in garnet pressure shadows. Th-Pb ages were obtained from monazite inclusions in garnet and in the matrix. Monazite inclusions yielded a weighted mean age of 220.1 ± 3.5 (MSWD = 0.8; n = 5). Matrix monazites produced a much wider spread in ages, from 208 to 21 Ma (Figure 3g). We interpret this range in matrix monazite ages to indicate partial resetting of Late Triassic metamorphic monazites during Oligocene shearing along the RRSZ. Monazite inclusions were not affected by this heating event due to shielding by their garnet hosts.

4.5.5. Ninh Binh Zone

[40] V-132 is a mylonitic gneiss from Ninh Binh, in the southernmost extension of the Day Nui Con Voi (Figure 2). Garnet porphyroblasts are elongate and commonly contain inclusions of quartz, biotite and K-feldspar, often with a higher density of inclusions in the garnet core. Biotite, chlorite, and muscovite are present in asymmetric pressure shadows around garnets. Matrix monazites yielded Th-Pb ages ranging smoothly from 107 to 32 Ma. The oldest monazites are significantly smaller in size than the younger grains, suggestive of new monazite growth by dissolution of preexisting monazite.

5. Thermobarometric Results

[41] In this section we outline the methods used to obtain and interpret P-T data from three high-grade rocks from the RRSZ. Compositional data from garnet, biotite, muscovite, plagioclase, and ilmenite used in thermobarometric calculations are listed in Table 3. X-ray element maps of garnets, garnet zoning profiles, and P-T plots for each sample are shown in Figures 4, 5, and 6.

5.1. P-T Estimates for the Diancang Shan

[42] Detailed electron microprobe analysis of a garnet-staurolite micaschist (DC-3) reveal zoning profiles in garnet that are bell-shaped, with concentrations of Mn and Ca that are high in the core and decrease toward the rim (Figures 4a and 4b). These zoning patterns suggest that most of the garnet's original composition is preserved. A slight increase in Mn and Fe/(Fe + Mg) at the extreme rim indicates minor ion exchange of Fe-Mg with biotite and/or garnet dissolution during retrogression [*Spear*, 1993; *Kohn and Spear*, 2000].

[43] The common practice of estimating peak metamorphic conditions by pairing the garnet composition with the lowest Mn and Fe/(Fe + Mg) content [*Florence and Spear*, 1991; *Spear*, 1991], typically at or near the garnet rim, with nearby matrix minerals could not be applied to DC-3 because all original matrix biotite has been altered or consumed during retrograde alteration. To attempt to determine peak temperatures, mineral inclusions were paired with the adjacent garnet. Application of the garnet-ilmenite thermometer [*Pownceby et al.*, 1987] yielded temperatures of 540-610°C for an ilmenite inclusion in the garnet core and temperatures of 480-550°C for an inclusion closer to the rim (Figure 4c). Because the highest temperature assem-

Table 3. Mineral Compositions Used in Thermobarometric Calculations

	Sample																											
	DC-3	DC-3	DC-3	DC-3	DC-3	DC-3	DC-3	DC-3	DC-3	YU-86	YU-86	YU-86	YU-86	YU-86	YU-86	YU-86	YU-86	YU-86	YU-86	YU-86	V-5	V-5	V-5	V-5	V-5	V-5	V-5	V-5
Mineral[a]	Gt	Gt	Gt	Gt	Gt	Bi	Bi	Ilm	Ilm	Gt	Gt	Bi	Bi	Bi	Bi	Msc	Msc	Plag	Plag	Plag	Gt	Gt	Gt	Bi	Bi	Bi	Ilm	Ilm
Position[b]	rim	rim	core	core	core	mat.	mat.	incl.	incl.	core	rim	mat.	mat.	incl.	incl.	mat.	mat.	mat.	mat.	incl.	core	core	rim	mat.	mat.	incl.	mat.	mat.
SiO_2	37.53	35.63	37.47	37.94	37.30	33.99	34.28	0.07	0.00	37.15	36.92	34.40	34.45	34.15	35.03	46.57	46.41	68.42	62.21	63.03	37.43	38.28	37.76	34.59	35.25	35.20	0.00	0.00
Mg0	2.33	2.18	2.48	2.37	2.38	10.04	11.48	0.46	0.44	4.14	2.50	7.70	7.47	8.46	8.53	0.60	0.99	0.00	0.00	0.00	4.49	4.77	4.01	7.63	7.38	8.65	0.79	0.36
Na_2O	0.00	0.01	0.00	0.00	0.00	0.09	0.07	0.00	0.00	0.00	0.00	0.13	0.14	0.09	0.07	0.41	0.46	7.75	8.75	8.64	0.00	0.00	0.00	0.13	0.13	0.29	0.00	0.00
Al_2O_3	21.34	19.84	21.21	21.26	21.18	18.99	19.16	0.08	0.03	21.07	20.60	18.66	19.88	17.15	18.21	35.67	35.40	20.43	23.34	24.62	21.01	21.59	21.40	18.61	18.01	18.48	0.00	0.04
FeO	33.67	33.20	32.34	31.43	31.56	17.89	19.91	45.22	45.55	34.27	34.36	20.80	19.77	19.00	19.25	1.36	2.34	0.07	0.21	0.39	34.05	33.82	35.62	20.84	21.59	18.05	46.94	44.91
MnO	4.59	4.53	5.01	5.25	4.89	0.09	0.09	0.92	1.08	1.24	3.93	0.17	0.18	0.05	0.15	0.05	0.02	0.05	0.01	0.00	0.50	0.55	0.84	0.05	0.03	0.09	0.16	0.21
Cr_2O_3	0.00	0.07	0.02	0.03	0.02	0.09	0.05	0.00	0.00	0.03	0.06	0.13	0.07	0.00	0.06	0.01	0.06	0.03	0.00	0.01	0.04	0.05	0.04	0.13	0.17	0.10	0.03	0.00
K_2O	0.00	0.02	0.00	0.00	0.00	9.30	7.64	0.02	0.00	0.02	0.01	9.13	9.48	9.52	9.09	9.69	10.52	0.07	0.29	0.16	0.00	0.00	0.00	9.59	9.41	9.73	0.01	0.00
CaO	1.93	1.80	3.09	3.38	3.19	0.12	0.11	0.03	0.00	1.36	1.11	0.04	0.00	0.02	0.04	0.00	0.00	4.42	4.63	5.41	1.93	1.94	2.12	0.00	0.02	0.04	0.04	0.00
TiO_2	0.00	0.01	0.07	0.08	0.08	1.30	0.93	53.59	53.92	0.02	0.01	2.89	2.90	4.40	3.83	0.22	0.16	0.02	0.00	0.02	0.00	0.02	0.05	4.54	5.20	5.79	52.35	52.52
Total	101.4	97.3	101.7	101.7	100.6	91.9	93.7	100.4	101.0	99.3	99.5	94.1	94.4	92.8	94.2	94.6	96.4	101.2	99.4	102.3	99.4	101.0	101.8	96.1	97.2	96.4	100.3	98.0
Si	2.99	2.99	2.98	3.00	2.99	5.35	5.28	0.00	0.00	2.99	3.01	5.36	5.32	5.37	5.39	6.20	6.14	2.95	2.77	2.74	3.00	3.01	2.98	5.28	5.33	5.29	0.00	0.00
Mg	0.28	0.27	0.29	0.28	0.28	2.36	2.64	0.02	0.02	0.50	0.30	1.79	1.72	1.98	1.96	0.12	0.20	0.00	0.00	0.00	0.54	0.56	0.47	1.74	1.66	1.94	0.03	0.01
Na	0.00	0.00	0.00	0.00	0.00	0.03	0.02	0.00	0.00	0.00	0.00	0.04	0.04	0.03	0.02	0.10	0.12	0.65	0.76	0.73	0.00	0.00	0.00	0.04	0.04	0.08	0.00	0.00
Al	2.01	1.96	1.99	1.98	2.00	3.52	3.48	0.00	0.00	2.00	1.98	3.42	3.62	3.18	3.30	5.60	5.52	1.04	1.23	1.26	1.98	2.00	1.99	3.35	3.21	3.27	0.00	0.00
Fe^{2+}	2.25	2.33	2.15	2.08	2.12	2.36	2.57	0.94	0.95	2.31	2.34	2.71	2.55	2.50	2.48	0.15	0.26	0.00	0.01	0.01	2.28	2.22	2.35	2.66	2.73	2.27	0.99	0.96
Mn	0.31	0.32	0.34	0.35	0.33	0.01	0.01	0.02	0.02	0.08	0.27	0.02	0.02	0.01	0.02	0.01	0.00	0.00	0.00	0.00	0.03	0.04	0.06	0.01	0.00	0.01	0.00	0.00
Cr	0.00	0.00	0.00	0.00	0.00	0.01	0.01	0.00	0.00	0.00	0.00	0.02	0.01	0.00	0.01	0.00	0.01	0.00	0.00	0.00	0.00	0.00	0.00	0.02	0.02	0.01	0.00	0.00
K	0.00	0.00	0.00	0.00	0.00	1.87	1.50	0.00	0.00	0.00	0.00	1.81	1.87	1.91	1.78	1.65	1.77	0.00	0.02	0.01	0.00	0.00	0.00	1.87	1.81	1.86	0.00	0.00
Ca	0.17	0.16	0.26	0.29	0.27	0.02	0.02	0.00	0.00	0.12	0.10	0.01	0.00	0.00	0.01	0.00	0.00	0.20	0.22	0.25	0.17	0.16	0.18	0.00	0.00	0.01	0.00	0.00
Ti	0.00	0.00	0.00	0.00	0.00	0.15	0.11	1.01	1.01	0.00	0.00	0.34	0.34	0.52	0.44	0.02	0.02	0.00	0.00	0.00	0.00	0.00	0.00	0.52	0.59	0.65	0.99	1.01
Total[c]	8.00	8.03	8.02	8.00	8.00	15.68	15.63	1.99	1.99	8.01	8.00	15.51	15.49	15.49	15.41	13.85	14.03	4.85	5.00	5.00	8.01	7.99	8.03	15.47	15.39	15.39	2.01	1.99
Fe/Fe+Mg	0.89	0.90	0.88	0.88	0.88	0.50	0.49	-	-	0.82	0.89	0.60	0.60	0.56	0.56	0.56	0.57	-	-	-	0.81	0.80	0.83	0.60	0.62	0.54	-	-
X_{Sps}	0.10	0.10	0.11	0.12	0.11	-	-	-	-	0.03	0.09	-	-	-	-	-	-	-	-	-	0.01	0.01	0.02	-	-	-	-	-
X_{Grs}	0.06	0.05	0.09	0.10	0.09	-	-	-	-	0.04	0.03	-	-	-	-	-	-	-	-	-	0.05	0.05	0.06	-	-	-	-	-
X_{Alm}	0.75	0.75	0.71	0.69	0.70	-	-	-	-	0.77	0.78	-	-	-	-	-	-	-	-	-	0.76	0.75	0.77	-	-	-	-	-
X_{Pyp}	0.09	0.09	0.10	0.09	0.09	-	-	-	-	0.17	0.10	-	-	-	-	-	-	-	-	-	0.18	0.19	0.15	-	-	-	-	-
X_{An}	-	-	-	-	-	-	-	-	-	-	-	-	-	-	-	-	-	0.24	0.23	0.26	-	-	-	-	-	-	-	-
X_{Ab}	-	-	-	-	-	-	-	-	-	-	-	-	-	-	-	-	-	0.76	0.77	0.74	-	-	-	-	-	-	-	-

[a]Minerals: Gt, garnet; Bi, biotite; Ilm, ilmenite; Msc, muscovite; Plag, plagioclase feldspar.
[b]Position: rim, garnet rim; core, garnet core; mat, rock matrix; incl, inclusion in garnet.
[c]Formulas are calculated on the basis of 12 oxygens for garnet, 22 oxygens for biotite and muscovite, 8 oxygens for plagioclase, and 3 oxygens for ilmenite.

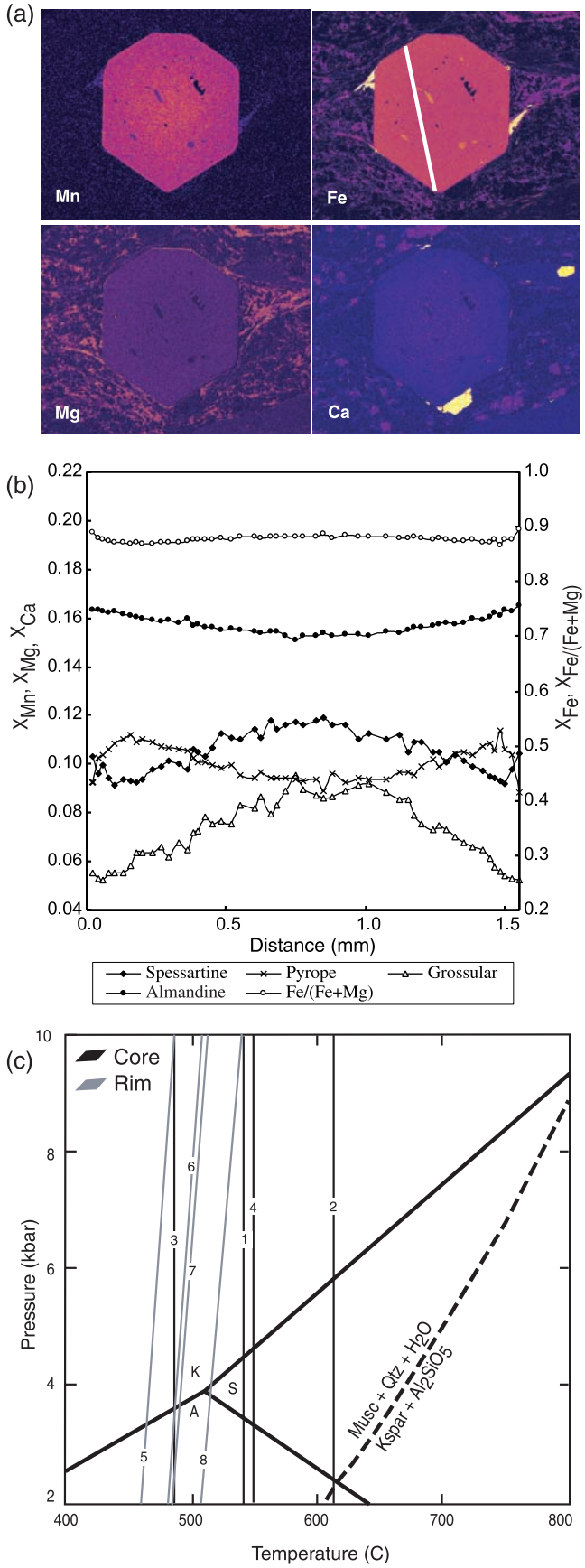

blage has been altered, these values represent minimum estimates for peak metamorphic temperatures.

[44] Retrograde conditions were estimated by pairing the garnet rim with nearby matrix biotite. The garnet-biotite thermometer yielded temperatures ranging from 460°C [*Hodges and Spear*, 1982] to 520°C [*Perchuk and Lavrent'eva*, 1984] for the pressure range 2–6 kbar (Figure 4c). Precise pressure estimates could not be obtained due to the lack of plagioclase. Previous P-T estimates for DC-3 based on modeling of compositional zoning patterns in garnets suggest a nearly isothermal evolution from 550°C and 7 kbar to 570°C and 5 kbar [*Leloup et al.*, 1993], broadly consistent with our results from the garnet core. Our rim thermometry (525 to 460°C) indicates somewhat lower temperatures, likely the result of continued local equilibration.

5.2. P-T Estimates for the Ailao Shan

[45] Garnet-sillimanite gneisses in the Ailao Shan typically exhibit a high degree of retrograde alteration. A zoning profile across an almandine garnet in sample YU-86 reveals concentrations of Mn and Fe/(Fe + Mg) that are relatively flat through the core but increase sharply at the rims (Figures 5a and 5b). Mg content decreases dramatically at the garnet rims, whereas Fe and Ca show very little zonation from core to rim. These zoning patterns suggest that the original growth zoning in this garnet has been destroyed by diffusional relaxation and retrograde net-transfer reactions [*Spear*, 1993]. Biotite in the matrix of the rock is slightly more Fe rich (Fe/Fe + Mg = 0.62) than biotite included in garnet (Fe/Fe + Mg = 0.55), consistent with biotite grown as a result of retrograde resorption of garnet [*Robinson*, 1991].

[46] Biotite inclusions in the core of the garnet were paired with the adjacent garnet to estimate metamorphic conditions during prograde garnet growth, yielding temperatures between 750 and 780°C (Figure 5c) [*Ferry and Spear*, 1978; *Berman*, 1990; *Hodges and Spear*, 1982]. Application of the garnet-muscovite-biotite-plagioclase-quartz barometer [*Hoisch*, 1990; *Hodges and Crowley*, 1985; *Powell and Holland*, 1988] and the garnet-sillimanite-plagioclase-quartz (GASP) barometer [*Hodges and Crowley*, 1985; *Newton and Haselton*, 1981] yielded a total

Figure 4. (opposite) (a) X-ray element map of Mn, Fe, Mg, and Ca of garnet from DC-3 from the southern Diancang Shan. Line shows location of traverse for compositional profile. High concentrations are shown in red, low concentrations in blue. (b) Chemical profiles across garnet from sample DC-3. (c) P-T results for sample DC-3. An ilmenite inclusion near the core of the garnet yields a peak temperature range of 540–610°C (1, *Ganguly and Saxena* [1984]; 2, *Pownceby et al.* [1987]), while an ilmenite inclusion in the outer core yields temperatures from 480–550°C (3, *Ganguly and Saxena* [1984]; 4, *Pownceby et al.* [1987]). A temperature range of 460–520°C (5, *Hodges and Spear* [1982]; 6, *Ferry and Spear* [1978] with *Berman* [1990]; 7, *Ganguly and Saxena* [1984]; 8, *Perchuk and Lavrent'eva* [1984]) is calculated by pairing the garnet rim with adjacent matrix biotite, for pressures of 2–6 kbar. The mineral assemblage precludes determination of a pressure for both peak and retrograde assemblages.

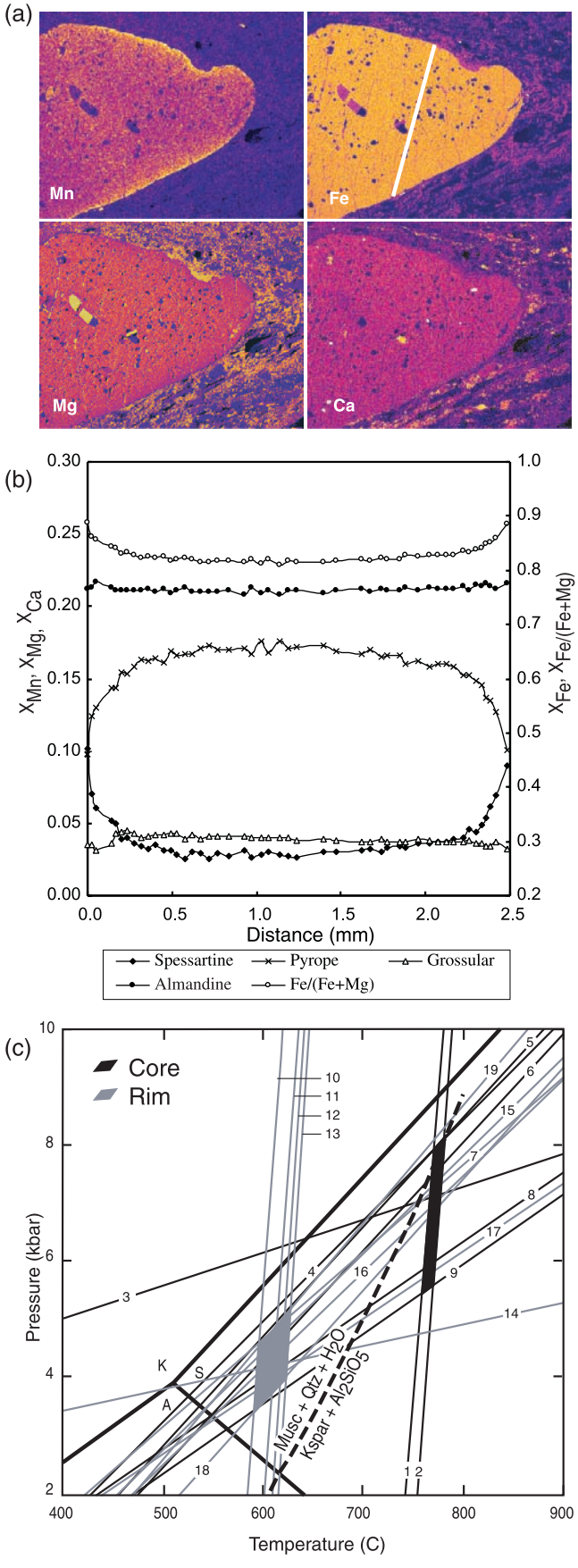

pressure range of 5.5–8.1 kbar. Retrograde biotite in the matrix paired with the garnet rim yielded temperatures of 580–625°C [*Ferry and Spear*, 1978; *Berman*, 1990; *Hodges and Spear*, 1982; *Ganguly and Saxena*, 1984; *Perchuk and Lavrent'eva*, 1984]. Pressures calculated for the garnet rim using the garnet-muscovite-biotite-plagioclase-quartz barometer [*Hoisch*, 1990; *Powell and Holland*, 1988; *Hodges and Crowley*, 1985] and the garnet-plagioclase-muscovite-quartz barometer [*Hoisch*, 1990; *Hodges and Crowley*, 1985] range from 3.5 to 5.2 kbar. The thermobarometric data indicate that YU-86 experienced upper amphibolite facies metamorphism, followed by a retrograde phase of lower amphibolite facies metamorphism.

[47] The extent of diffusional homogenization and partial dissolution experienced by garnets in this sample complicates interpretation of thermobarometric results. Nevertheless, the temperatures calculated for YU-86 are consistent with the mineral assemblage (i.e., the presence of sillimanite and K-feldspar), arguing undeniably for high peak temperatures. *Spear* [1991] calculated the penetration distance of Fe-Mg diffusion in garnet based on peak temperature, rate of cooling from high temperature, and garnet size. For the 1.2 mm diameter garnets in YU-86, peak temperatures of >650°C potentially permit diffusive exchange within the garnet core [*Spear*, 1991] and are within the range previously documented for peak metamorphic conditions in the Ailao Shan.

[48] Previous thermobarometry on sillimanite-garnet-gneisses from the northeastern margin of the Ailao Shan indicate peak metamorphic conditions of 710 ± 70°C and 4.5 ± 1.5 kbar, and retrograde conditions of ~500°C and <3.8 kbar [*Leloup and Kienast*, 1993]. The thermobarometric evolution evidenced by all P-T results from YU-86 are consistent with peak conditions of ~750°C and ~6 kbar and retrograde conditions of 600–500°C and ~4 kbar.

5.3. P-T Estimates for the Day Nui Con Voi

[49] Compositions of garnet, biotite, and ilmenite were used to calculate P-T conditions of metamorphism from

Figure 5. (opposite) (a) X-ray element map of Mn, Fe, Mg, and Ca of garnet from YU-86 from the central Ailao Shan. Line shows location of traverse for compositional profile. High concentrations are shown in yellow, low concentrations in blue. (b) Chemical profiles across garnet from sample YU-86 (c) P-T results for sample YU-86. Biotite inclusions paired with adjacent garnet yield a peak temperature range of 760–780°C (1, *Ferry and Spear* [1978] with *Berman* [1990]; 2, *Hodges and Spear* [1982]). The gt-ms-bt-pl-qz barometer (3, *Powell and Holland* [1988]; 4, *Hodges and Crowley* [1985]; 5, *Hoisch* [1990]) and GASP barometer (6, *Newton and Haselton* [1981]; 7, *Hodges and Crowley* [1985]; 8, *Hodges and Spear* [1982]; 9, *Ganguly and Saxena* [1984]) yield peak pressures of 5.5–8.1 kbar. Matrix biotite paired with the garnet rim yield retrograde temperatures of 580–625°C (10, *Perchuk and Lavrent'eva* [1984]; 11, *Ferry and Spear* [1978] with *Berman* [1990]; 12, *Ganguly and Saxena* [1984]; 13, *Hodges and Spear* [1982]). The gt-ms-bt-pl-qz barometer (14, *Powell and Holland* [1988]; 15, *Hodges and Crowley* [1985]; 16, *Hoisch* [1990]) and gt-pl-ms-qz (17, *Hoisch* [1990]; 18,19, *Hodges and Crowley* [1985]) barometer constrain pressures along the retrograde path between 3.5 and 5.2 kbar.

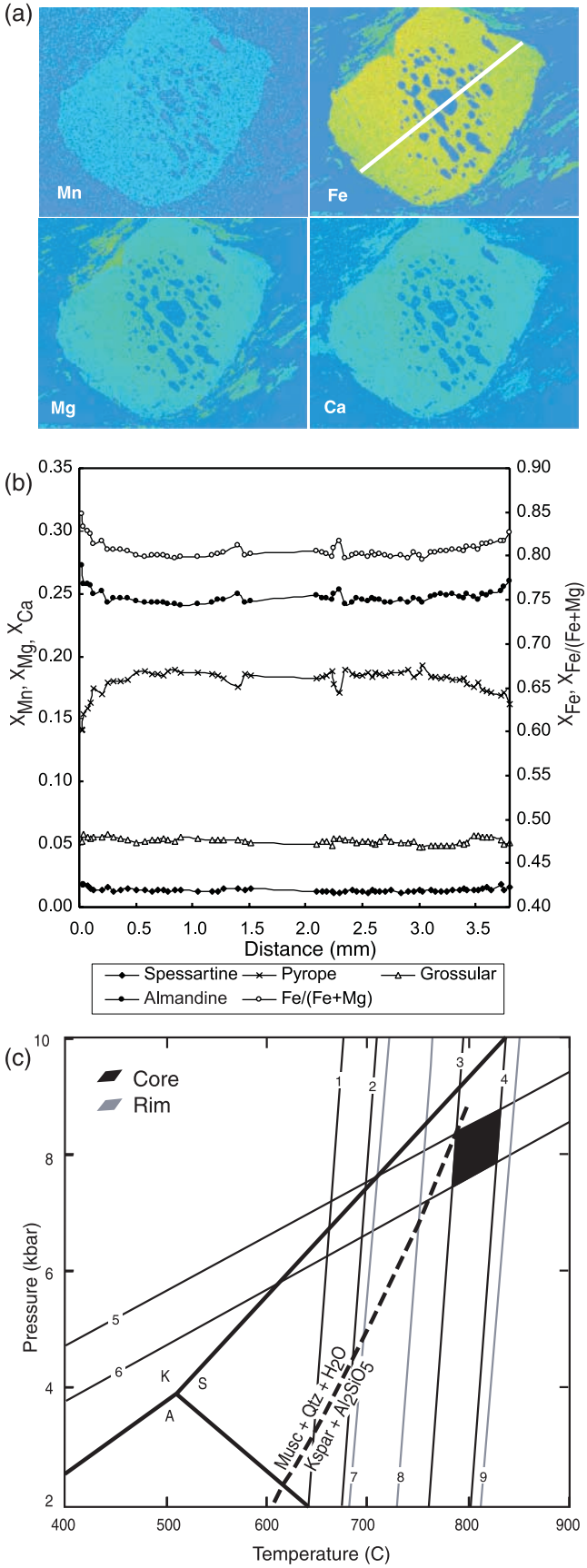

sample V-5, a garnet-sillimanite micaschist from the core of the Day Nui Con Voi. A traverse across a 3.8 mm diameter garnet reveals relatively flat compositional profiles with increasing Fe/(Fe + Mg) and decreasing Mg contents at the rims, indicative of high-temperature diffusional homogenization (Figures 6a and 6b). No abrupt chemical change was observed across the transition from inclusion-rich core to inclusion-free rim, arguing against multiple episodes of garnet growth.

[50] P-T conditions of garnet growth were estimated by pairing the core with biotite, sillimanite, ilmenite and rutile inclusions. The garnet-biotite thermometer [*Ferry and Spear*, 1978; *Berman*, 1990; *Hodges and Spear*, 1982] in combination with the GRAIL barometer [*Bohlen et al.*, 1983] yields conditions for the core of 780–830°C and 7.5–8.8 kbar (Figure 6c). Conditions along the retrograde path were determined by pairing the garnet rim, although altered by diffusion and retrograde exchange reactions, with adjacent matrix biotite yielding temperatures from 680°C [*Perchuk and Lavrent'eva*, 1984] to 840°C [*Ferry and Spear*, 1978; *Berman*, 1990] for the pressure range 2–8 kbar. The matrix mineral assemblage in V-5 is unsuitable for barometric analysis, precluding calculation of a pressure for retrograde conditions.

[51] The elevated P-T conditions for V-5 are in agreement with the mineral assemblage and the observation that these garnets experienced temperatures high enough to completely erase their original growth zoning. *Spear* [1991] has suggested that temperatures in excess of 825°C would be necessary for diffusion to penetrate to the core of a ~4 mm diameter garnet, in agreement with our results. Previous estimates of P-T conditions for the Day Nui Con Voi (including samples V-1, V-12, and V-132) suggest somewhat lower peak temperatures. *Leloup et al.* [2001] report peak P-T conditions of 735 ± 65°C and 4.7 ± 1.7 kbar. Minerals in garnet pressure shadows, developed during sinistral deformation, yielded retrograde conditions of 655 ± 75°C and 3.5 ± 1.0 kbar [*Leloup et al.*, 2001]. *Nam et al.* [1998]

Figure 6. (opposite) (a) X-ray element map of Mn, Fe, Mg, and Ca of garnet from V-5. Line shows location of traverse for compositional profile. High concentrations are shown in yellow, low concentrations in blue. (b) Chemical profiles across garnet from sample V-5, from the central Day Nui Con Voi. (c) P-T results for sample V-5 from the central Day Nui Con Voi. Biotite inclusions paired with adjacent garnet yield a peak temperature range of 780–830°C (1, *Ganguly and Saxena* [1984]; 2, *Perchuk and Lavrent'eva* [1984]; 3, *Ferry and Spear* [1978] with *Berman* [1990]; 4, *Hodges and Spear* [1982]). Because the core assemblage is in equilibrium with sillimanite and K-feldspar, equilibria 1 and 2 are disregarded. The gt-rt-sill-ilm-qz (GRAIL) barometer constrains pressures between 7.5 and 8.8 kbar (5, *Bohlen et al.* [1983]; 6, *Bohlen et al.* [1983]). Pairing of the garnet rim with adjacent matrix biotite yields a temperature range of ~680–840°C for the retrograde rim assemblage (7, *Perchuk and Lavrent'eva* [1984]; 8, *Ganguly and Saxena* [1984]; 9, *Ferry and Spear* [1978] with *Berman* [1990]). The matrix assemblage precludes determination of a pressure along the retrograde path.

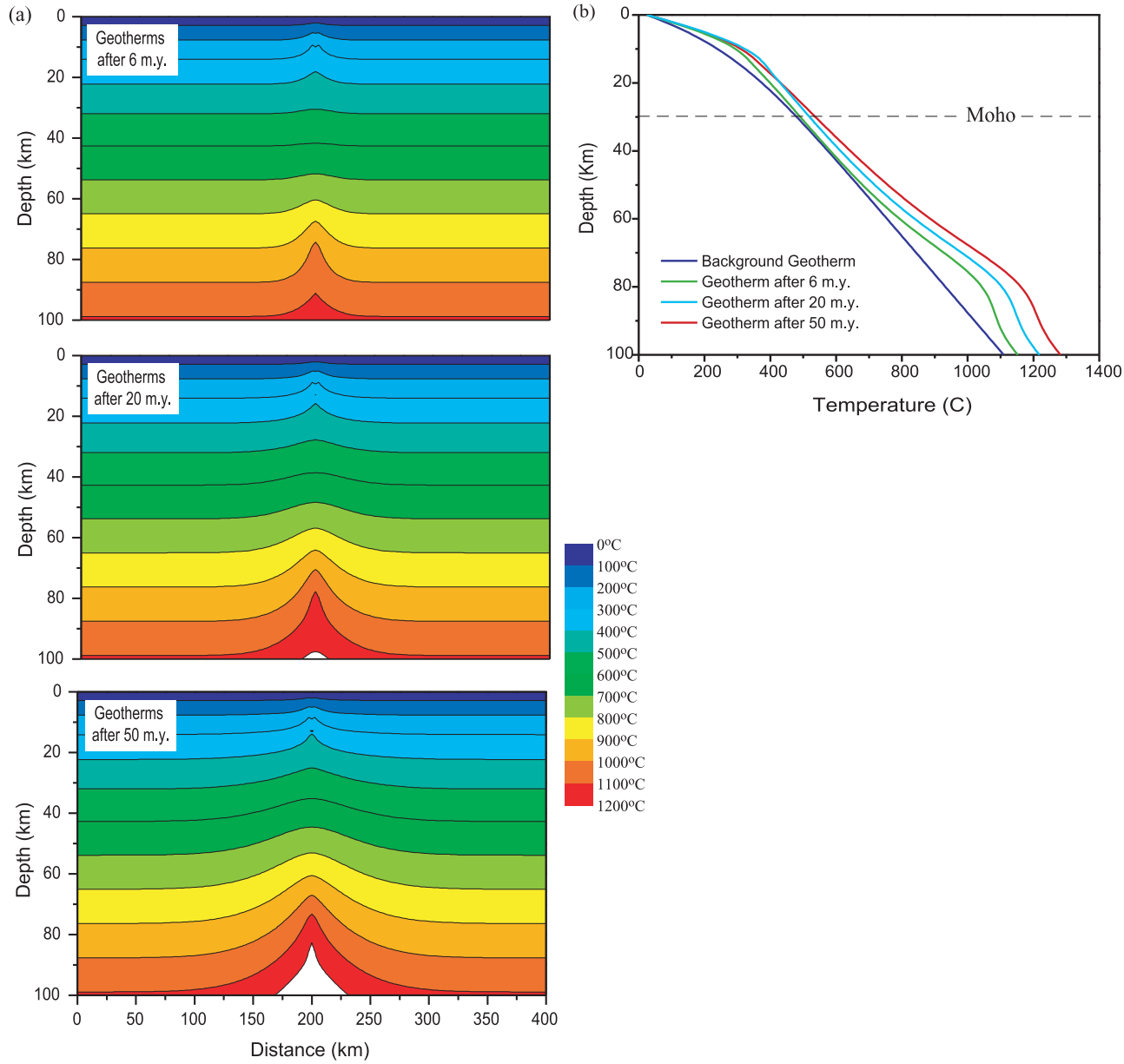

Figure 7. Results from a finite difference, conductive model for shear heating in the RRSZ. Shear zone is 10 km wide normal to the plane of the page. Depth to brittle-ductile transition is set as 12 km; Moho is at 30 km. All other thermal and mechanical parameters follow *Leloup et al.* [1999]. (a) Geotherms after 6, 20, and 50 m.y. of shearing at 4 cm/yr. Results suggest that at least ~20 m.y. are necessary to reach steady state conditions in the middle crust. (b) After 20 m.y. of shearing the temperature in the middle crust increases by only 60–80°C, insufficient to explain the high metamorphic temperatures recorded by rocks in the Ailao Shan.

reports peak pressures and temperatures of 690 ± 30°C and 6.5 ± 1.5 kbar for micaschists from the Day Nui Con Voi, followed by mylonitization at 480 ± 80°C and <4 kbar. Together, the thermobarometric data suggest that garnet growth occurred along a clockwise P-T path.

6. Discussion

6.1. Summary of P-T-t Data

[52] While diffusive Pb loss might partially reset the U-Th-Pb isotopic system in monazites exposed to prolonged, high temperature (>650°C) heating events, once monazite is encompassed by a growing garnet it can be effectively armored against Pb loss [e.g., *Harrison et al.*, 1987; *Montel et al.*, 2000; *Foster et al.*, 2000; *Catlos et al.*, 2001]. Thus Th-Pb ages of monazites included within prograde garnets may in certain cases be interpreted to date prograde garnet growth. Integration of such geochronologic data with thermobarometric constraints derived from selected garnet-bearing samples enables us to decipher the P-T-t history of metamorphism in the RRSZ and directly constrain the timing of shearing and high-temperature metamorphism.

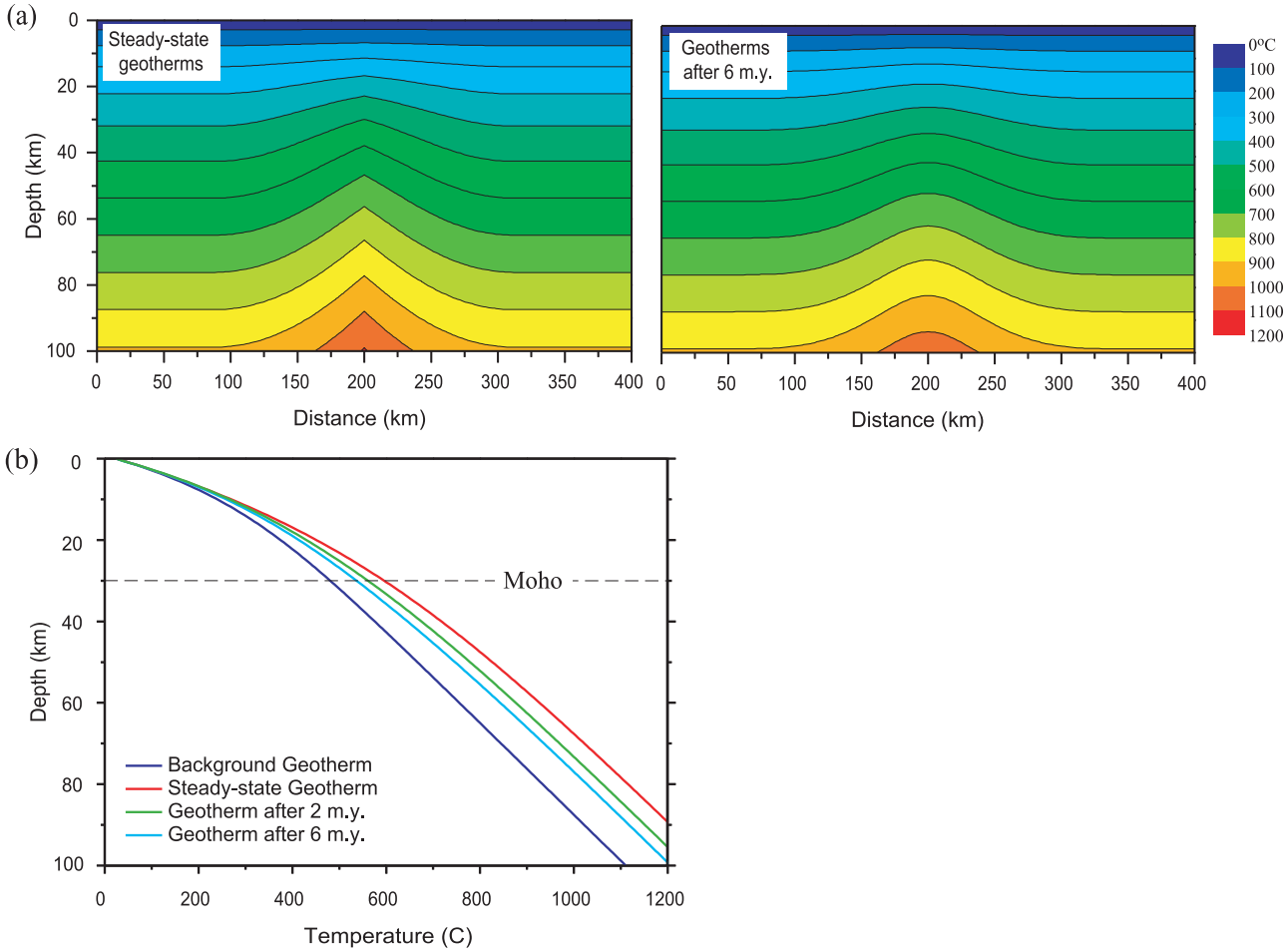

Figure 8. Results from finite difference, conductive model for relaxation of perturbed geotherm after steady state conditions are reached. Shear zone is 10 km wide normal to the plane of the page. Depth to brittle-ductile transition is set as 12 km; Moho is at 30 km. All other parameters follow *Leloup et al.* [1999]. (a) Geotherms under steady state conditions of shearing at 4 cm/yr and geotherms 6 m.y. after the cessation of shearing. (b) Relaxation of geothermal gradient.

[53] Th-Pb monazite geochronology yields similar age ranges for the Xuelong Shan, Diancang Shan, and Ailao Shan. In the Xuelong Shan, matrix monazite grains range from 25 to 19 Ma and in the Diancang Shan the majority cluster between 28 and 25 Ma. These observed age ranges are interpreted to reflect protracted high-temperature metamorphism during shearing along the RRSZ.

[54] Monazite inclusions in metapelitic rocks from the Ailao Shan date garnet growth between 34 and 21 Ma, while matrix monazites range from 74 Ma to 16 Ma. We interpret the late Cretaceous-early Tertiary ages to represent partial resetting of preexisting monazite during Oligocene deformation along the RRSZ. The Oligocene-early Miocene ages thus likely reflect growth of metamorphic monazite through dissolution of inherited grains. Thermobarometric analysis of a high-grade garnet-sillimanite gneiss from the eastern Ailao Shan indicates peak metamorphic conditions of ~750°C and ~6 kbar. These results corroborate previous work [e.g., *Leloup et al.*, 1993; *Leloup and Kienast*, 1993].

[55] Geochronological results from the Day Nui Con Voi are strikingly different from the other ranges. Monazite ages for inclusions in garnet range from ~220 to 44 Ma, while matrix monazites are as young as ~21 Ma. We interpret the older monazites to be remnants of a Triassic metamorphic assemblage, partially to completely reset during mid-Tertiary shearing along the RRSZ. The timing of the high temperature event responsible for monazite age resetting is not precisely constrained, but must be of Tertiary age, possibly as young as 21 Ma.

[56] The survival of >200 Ma matrix monazites at apparent temperatures of ~800°C is consistent with the Pb diffusion behavior observed by *Cherniak et al.* [2000] and geological evidence suggesting that monazite can retain part or all of its Pb through upper amphibolite-grade metamorphism [*Parrish*, 1990; *Montel et al.*, 2000; *Foster et al.*, 2000; *Rubatto et al.*, 2001; *Cherniak and Watson*, 2000]. However, monazites unprotected by garnet hosts are susceptible to Pb loss via recrystallization. For sample V-5, from which the aforementioned thermometry was calculated, matrix monazites were all Oligocene in age and only monazite inclusions gave older ages. Most of the samples dated from the Day Nui Con Voi come from the eastern margin of the massif, whereas V-5 was collected from the core. Because the Day Nui Con Voi forms an antiformal

dome, samples from the core of the massif represent lower structural levels and presumably record hotter temperatures. P-T paths for these samples need to be calculated and integrated with the age data before we can be confident what temperatures these partially reset monazites were exposed to. Another possibility is that the P-T estimates dominantly reflect the conditions of the Indosinian orogeny (see results for Song Chay dome), but that peak Tertiary metamorphism did not reach such elevated temperatures. Because of the ambiguity in the peak P-T conditions experienced by samples from the Day Nui Con Voi, and in the timing represented by these conditions, geochronologic and thermobarometric results from the Day Nui Con Voi are not integrated into our tectonic model for the evolution of the RRSZ.

6.2. Tectonic Implications

[57] The Tertiary tectonic evolution of the RRSZ, in particular its kinematic relationship with the opening of the South China Sea, is a key prediction of the hypothesis that extrusion of Indochina has accommodated a significant portion of the Indo-Asian convergence. Thermochronological data from the RRSZ have already established that the rate at which transtensional faulting propagated from SE to NW in the Ailao Shan (~4 cm/yr [*Harrison et al.*, 1996]) falls within the known range of seafloor spreading [*Briais et al.*, 1993]. Assuming a delay of 2–4 m.y. from the initiation of shearing to the onset of seafloor rifting, the extrusion model predicts the onset of left-lateral shearing on the RRSZ at about 33–35 Ma.

[58] The geochronologic results presented in this study are the first to directly date high-temperature metamorphism and left-lateral shearing along the RRSZ. The period of left-lateral deformation now documented along the RRSZ (i.e., 34–17 Ma) [*Harrison et al.*, 1996; *Leloup et al.*, 2001; this study] is coincident with the timing derived from magnetic anomalies in the South China seafloor (i.e., 30.5–17 Ma) [*Briais et al.*, 1993; *Berggren et al.*, 1995]. These new age constraints thus provide strong evidence in support of the interpretation that the South China Sea opened as a pull-apart basin as a result of left-lateral movement on the RRSZ. The results further strengthen the view that extrusion of continental blocks along lithospheric-scale strike-slip faults accommodated a significant amount of the convergence between India and Asia [e.g., *Tapponnier et al.*, 1982, 1986; *Briais et al.*, 1993; *Leloup et al.*, 1995, 2001; *Harrison et al.*, 1996].

6.3. Heat Sources for Metamorphism

[59] The heat source for high-temperature metamorphism and anatexis in strike-slip shear zones within unthickened crust remains controversial. *Leloup et al.* [1993, 1995] proposed that the apparent thermal anomaly observed in the RRSZ resulted largely from shear heating. However, other workers questioned whether this mechanism could provide sufficient heat due to the negative feedback between temperature and rock strength [*Brun and Cobbold*, 1980; *Fleitout and Froidevaux*, 1980; cf. *England and Molnar*, 1993]. To investigate the role of shear heating in general, and in the RRSZ in particular, *Leloup et al.* [1999] constructed a steady state conductive model to describe the distribution of heat within and adjacent to a lithospheric, strike-slip shear zone. In their finite difference model, heat generation is concentrated immediately above the brittle-ductile transition and just below the Moho where rock strengths are at a maximum. For a shear zone with a peak flow stress of ~200 MPa slipping at 4 cm/yr, *Leloup et al.* [1999] concluded that shear heating alone could elevate the midcrustal geotherm by as much as 150°C. However, midcrustal rocks residing at temperatures below the garnet isograd (~500°C) prior to the onset of Tertiary metamorphism, when peak temperatures reached >700°C in places, require a temperature increase of ≥200°C. Assuming that heat transport occurs only by conduction, significant time would be required for this increase in temperature to be attained.

[60] Geochronologic data from the RRSZ, including anatectic leucogranites (25–22 Ma [*Schärer et al.*, 1994; *Zhang and Schärer*, 1999]) and monazite inclusions in deformed garnets (34–21 Ma; this study) indicate that high temperatures were apparently maintained at midcrustal depths for up to 10 m.y. This extended duration of high-temperature metamorphism was used by *Leloup et al.* [1999] to justify the assumption of steady state conditions in developing their thermomechanical model. On the assumption that the thermal time constant for a shear zone environment can be characterized by the 1-D approximation $x = \sqrt{\kappa t}$ (where κ is thermal diffusivity), they argued that the vertical separation of maximum heat generation between the brittle-ductile transition at ~15 km and Moho at ~35 km justifies a scale length of order 10 km. This in turn corresponds to a thermal time constant of ~4 m.y. (for $\kappa = 10^{-6}$ m^2/s). *Leloup et al.* [1999, p. 23] viewed this as a maximum value for the attainment of steady state conditions as "the shear stress, and hence heat production, is greater at the beginning of deformation when temperatures are lower". However, this assumption appears flawed as the thermal problem is fully 2-D and thus involves significant lateral heat flow (i.e., the 1-D approximation underestimates the time for attainment of steady state conditions). Furthermore, the use of power law-type rheologies [*Leloup et al.*, 1999] introduces a non-linear nature into these calculations which, unless fully investigated, could yield incorrect solutions.

[61] We have used a time-dependent, conductive thermal model and the thermal and mechanical parameters and boundary conditions of *Leloup et al.* [1999] to investigate (1) the time delay after initiation of shearing before amphibolite-facies conditions would be experienced in the middle crust and (2) the time necessary after the cessation of shearing for the perturbed geotherm to relax back to its initial value. The diffusion equation was solved numerically using a 2-D Crank-Nicholson finite difference method (both direct and alternating-direction implicit techniques) while shear and radiogenic heating were calculated using a direct method [*Press et al.*, 1988]. Constant temperature (25°C) was maintained at the surface while constant flux (q_m = 20 μW/m^2) was imposed at the bottom (z = 100 km). Heat production due to radioactivity was assumed to decrease exponentially with depth according to $H = H_S e^{-z/h_r}$, where H_S is the radiogenic heat production rate per unit mass, z is depth, h_r (= 10 km) is the characteristic length scale for the decrease in H with depth, and $\rho H_S = (q_s - q_m)/h_r$ = 3 μW/m^3, where ρ is rock density and q_s is surface heat flow [*Turcotte and Schubert*, 1982].

[62] Shear heating on a vertical boundary with an imposed horizontal velocity of 4cm/yr was approximated following *Leloup et al.* [1999] with some simplifications. The brittle-ductile transition zone was set at 12 km depth and the Moho at 30 km. A peak shear stress of 200 MPa is reached at 12 km and decreases linearly to zero at 30 km. Below the Moho, shear stress increases to 100 MPa and drops to zero at 100 km depth. Heat production in the brittle zone was calculated in the same fashion as by *Leloup et al.* [1999]. Strain heat production in the ductile zone and lower mantle was calculated from the expression $Q_{f(x,z)} = A\tau_{d(z)}^{N+1}\exp(-E/RT_{(x,z)})$ [*Leloup et al.*, 1999, equation 10], with two approximations. First, the shear stress was linearly approximated from Figure 2 of *Leloup et al.* [1999]. Second, shear heating was assumed to be independent of the lateral distribution (x) of temperature, with heat generation occurring only within a 1 km wide zone across the fault. In order to avoid the runaway instability introduced by this approach (i.e., rising temperatures implying rising shear heating), we used a constant geotherm far from the fault zone to calculate the shear heating [*Leloup et al.*, 1999, equation 10] effectively making the shear heat production approximately constant through the calculation. These approximations are unlikely to negatively influence comparisons between the two models, although our results may tend to overestimate the temperature rise. Note that because there is no feedback between flow stress and temperature, our results represent an upper limit to the possible temperature increase.

[63] Results from forward modeling of the conditions appropriate to the RRSZ suggest that ca. 20 m.y. is necessary to attain steady state conditions in the middle crust after the onset of shearing (Figure 7), much longer than predicted by *Leloup et al.* [1999]. After 5 m.y. of shear heating, midcrustal temperatures are elevated by only 30–40°C; after 20 m.y. temperatures will be raised by 60–80°C. Thus the differential temperature arising from shear heat production alone is not sufficient to explain the high metamorphic temperatures (~750°C) recorded by rocks in the Ailao Shan, assuming these midcrustal rocks were below the garnet isograd (~500°C) prior to the onset of Tertiary metamorphism. This requires another heat source(s) to have played the dominant role in generating midcrustal amphibolite-facies conditions. The most likely alternative source comes from melts ascending through the shear zone that were derived from mantle heating resulting from either shear heating [*Leloup et al.*, 1999] or continental subduction [*Wang et al.*, 2001]. This hypothesis is supported by the widespread presence of 42 to 24 Ma calc-alkaline volcanic and intrusive rocks along the entire length of the RRSZ [e.g., *Wang et al.*, 2001]. Advective transport of heat via rising magmas could significantly raise temperatures in the upper levels of the shear zone, increasing both the vertical and horizontal thermal gradients [*Leloup et al.*, 1999]. After the cessation of shearing, our modeling shows that ~50 m.y. is required for the steady state geotherm to relax to close to its initial value (Figure 8).

7. Conclusions

[64] The thermobarometric and geochronologic data presented in this study constrain the timing of prograde metamorphism and left-lateral deformation within the RRSZ. Our results indicate that the rocks exposed at the surface in the Diancang Shan did not experience temperatures as high as those affecting rocks in the Ailao Shan and Day Nui Con Voi, in agreement with previous studies [e.g., *Leloup and Kienast*, 1993; *Leloup et al.*, 1993; 2001]. The physical conditions experienced within the Day Nui Con Voi during Tertiary strike-slip faulting are obscured by amphibolite-grade metamorphism, which had previously been achieved during the Indosinian orogeny. A precise understanding of the Tertiary metamorphic conditions in the Day Nui Con Voi will require a more detailed P-T-t study of this terrane.

[65] Time-dependant thermal modeling suggests that shear heating in the RRSZ was transient, and did not attain steady state conditions as previously proposed [*Leloup et al.*, 1999]. Shear heating alone appears to be insufficient to bring about the >200°C temperature rise observed in rocks from the middle crust. We attribute the large temperature rise to magmas ascending through the shear zone during the main phase of left-lateral shearing.

[66] Th-Pb ion microprobe analyses of monazite inclusions in syntectonic garnets from the Ailao Shan date prograde metamorphism and left-lateral ductile deformation within the RRSZ between 34 and 21 Ma. Combined with previous thermochronological results [*Harrison et al.*, 1996], the new monazite age data presented here demonstrate that the timing of left-lateral shearing along the RRSZ (i.e., 34–17 Ma) overlaps with seafloor spreading in the South China Sea (i.e., 30.5–17 Ma) [*Briais et al.*, 1993; *Berggren et al.*, 1995]. The coincidence in the timing of these two events strengthens the hypothesis that the opening of the South China Sea was driven by left-lateral strike-slip faulting on the RRSZ.

[67] **Acknowledgments.** This research was conducted with support from the Institute of Geophysics and Planetary Physics- Lawrence Livermore National Laboratory UCRP 00-GS017 and from the Instrumentation and Facilities Program of the National Science Foundation. We thank E. Catlos and D. Stockli for helpful discussions and C. Coath and G. Jarzebinski for technical assistance with ion microprobe and SEM analysis. We also thank N. Mancktelow, D. Foster, and S. van der Lee for constructive reviews. This paper is IPGP contribution 1825.

References

Berggren, W. A., K. V. Kent, M. P. Aubry, and J. Hardenbol, A revised Cenozoic geochronology and chronostratigraphy, in *Geochronology, Time Scales and Global Stratigraphic Correlation*, edited by W. A. Berggren et al., *Spec. Publ. Soc. Sediment. Geol.*, *54*, 129–212, 1995.

Berman, R. G., Mixing properties of Ca-Mg-Fe-Mn garnets, *Am. Mineral.*, *75*, 328–344, 1990.

Bohlen, S. R., V. J. Wall, and A. L. Boettcher, Experimental investigations and geological applications of equilibria in the system FeO-TiO_2-Al_2O_3-SiO_2-H_2O, *Am. Mineral.*, *68*, 1049–1058, 1983.

Briais, A., P. Patriat, and P. Tapponnier, Updated interpretation of magnetic anomalies and seafloor spreading stages in the South China Sea: Implications for the Tertiary tectonics of Southeast Asia, *J. Geophys. Res.*, *98*, 6299–6328, 1993.

Brun, J. P., and P. R. Cobbold, Strain heating and thermal softening in continental shear zones: A review, *J. Struct. Geol.*, *2*, 149–158, 1980.

Catlos, E. J., T. M. Harrison, M. J. Kohn, M. Grove, F. J. Ryerson, C. E. Manning, and B. N. Upreti, Geochronologic and thermobarometric constraints on the evolution of the Main Central Thrust, central Nepal Himalayan, *J. Geophys. Res.*, *106*, 16,177–16,204, 2001.

Cherniak, D. J., and E. B. Watson, Pb diffusion in zircon, *Chem. Geol.*, *172*, 5–24, 2000.

Cherniak, D. J., E. B. Watson, T. M. Harrison, and M. Grove, Pb diffusion in monazite: A progress report on a combined RBS/SIMS, *Eos Trans. AGU*, *81*(19), Spring Meet. Suppl., Abstract GS31A-03, 2000.

Dewey, J. F., S. Cande, and W. C. Pitman, Tectonic evolution of the India/Eurasia collision zone, *Eclogae Geol. Helv.*, *82/3*, 717–734, 1989.

England, P., and G. Houseman, Finite strain calculations of continental deformation, 2, Comparison with the India-Asia collision zone, *J. Geophys. Res.*, *91*, 3664–3676, 1986.

England, P., and P. Molnar, The interpretation of inverted metamorphic isograds using simple physical calculations, *Tectonics*, *12*, 145–157, 1993.

Ferry, J. M., and F. S. Spear, Experimental calibration of partitioning of Fe and Mg between biotite and garnet, *Contrib. Mineral. Petrol.*, *66*, 113–117, 1978.

Fleitout, L., and C. Froidevaux, Thermal and mechanical evolution of shear zones, *J. Struct. Geol.*, *2*, 159–164, 1980.

Florence, S. P., and F. S. Spear, Effects of diffusional modification of garnet growth zoning on P-T path calculations, *Contrib. Mineral. Petrol.*, *107*, 487–500, 1991.

Foster, G. L., P. Kinny, D. Vance, C. Prince, and N. Harris, The significance of monazite U-Th-Pb age data in metamorphic assemblages: A combined study of monazite and garnet chronometry, *Earth Planet. Sci. Lett.*, *181*, 327–340, 2000.

Ganguly, J., and S. K. Saxena, Mixing properties of aluminosilicate garnets: Constraints from natural and experimental data, and applications to geothermo-barometry, *Am. Mineral.*, *69*, 88–97, 1984.

Gilley, L. D., Timing of left-lateral shearing and prograde metamorphism along the Red River shear zone, China and Vietnam, M. S. Thesis, 299 pp., Univ. of Calif., Los Angeles, 2001.

Harrison, T. M., C. Wenji, P. H. Leloup, F. J. Ryerson, and P. Tapponnier, An early Miocene transition in deformation regime within the Red River fault zone, Yunnan, and its significance for Indo-Asian tectonics, *J. Geophys. Res.*, *97*, 7159–7182, 1992.

Harrison, T. M., K. D. McKeegan, and P. LeFort, Detection of inherited monazite in the Manaslu leucogranite by $^{208}Pb/^{232}Th$ ion microprobe dating: Crystallization age and tectonic implications, *Earth Planet. Sci. Lett.*, *133*, 271–282, 1995.

Harrison, T. M., P. H. Leloup, F. J. Ryerson, P. Tapponnier, and C. Wenji, Diachronous initiation of transtension along the Ailao Shan-Red River shear zone, Yunnan and Vietnam, in *The Tectonic Evolution of Asia*, edited by A. Yin and T. M. Harrison, pp. 208–206, Cambridge Univ. Press, New York, 1996.

Harrison, T. M., F. J. Ryerson, P. LeFort, A. Yin, O. M. Lovera, and E. J. Catlos, A late Miocene-Pliocene origin for central Himalayan inverted metamorphism, *Earth Planet. Sci. Lett.*, *146*, E1-8, 1997.

Harrison, T. M., M. Grove, K. D. McKeegan, C. D. Coath, O. M. Lovera, and P. Le Fort, Origin and episodic emplacement of the Manaslu intrusive complex Central Himalaya, *J. Petrol.*, *40*, 3–19, 1999.

Hodges, K. V., and P. D. Crowley, Error estimation and empirical geothermobarometry for pelitic systems, *Am. Mineral.*, *70*, 702–709, 1985.

Hodges, K. V., and F. S. Spear, Geothermometry, geobarometry and the Al_2SiO_5 triple point at Mt. Moosilauke, New Hampshire, *Am. Mineral.*, *67*, 1118–1134, 1982.

Hoisch, T. D., Empirical calibration of six geobarometers for the mineral assemblage quartz + muscovite + biotite + plagioclase + garnet, *Contrib. Mineral. Petrol.*, *104*, 225–234, 1990.

Houseman, G., and P. England, Crustal thickening versus lateral extrusion in the Indian-Asian continental collision, *J. Geophys. Res.*, *98*, 12,233–12,249, 1993.

Kohn, M. J., and F. Spear, Retrograde net transfer reaction insurance for pressure-temperature estimates, *Geology*, *28*, 1127–1130, 2000.

Köppel, V., A. Gunthert, and M. Grünenfelder, Patterns of U-Pb zircon and monazite ages in polymetamorphic units or the Swiss Central Alps, *Schweiz. Mineral. Petrogr. Mitt.*, *61*, 97–119, 1980.

Leloup, P. H., and J. R. Kienast, High temperature metamorphism in a major strike-slip shear zone: The Ailao Shan-Red River (PRC), *Earth Planet. Sci. Lett.*, *118*, 213–234, 1993.

Leloup, P. H., T. M. Harrison, F. J. Ryerson, C. Wenji, Q. Li, P. Tapponnier, and R. Lacassin, Structural, petrological and thermal evolution of a Tertiary ductile strike-slip shear zone Diancang Shan, Yunnan, *J. Geophys. Res.*, *98*, 6715–6743, 1993.

Leloup, P. H., R. Lacassin, P. Tapponnier, U. Schärer, Z. Dalai, L. Xiaohan, Z. Liangshang, J. Shaocheng, and P. T. Trinh, The Ailao Shan-Red River shear zone (Yunnan China), Tertiary transform boundary of Indochina, *Tectonophysics*, *25*, 3–84, 1995.

Leloup, P. H., Y. Ricard, J. Battaglia, and R. Lacassin, Shear heating in continental strike-slip shear zones: Model and field examples, *Geophys. J. Int.*, *136*, 19–40, 1999.

Leloup, P. H., N. Arnaud, R. Lacassin, J. R. Kienast, T. M. Harrison, P. T. Trinh, A. Replumaz, and P. Tapponnier, New constraints on the structure, thermochronology and timing of the Ailao Shan-Red River shear zone SE Asia, *J. Geophys. Res.*, *106*, 6683–6732, 2001.

Maluski, H., C. Lepvrier, L. Jolivet, A. Carter, D. Roques, O. Beyssac, T. T. Tang, N. D. Thang, and D. Avigard, Ar-Ar and fission-track ages in the Song Chay massif: Early Triassic and Cenozoic tectonics in northern Vietnam, *J. Southeast Asian Earth Sci.*, *19*, 233–248, 2001.

Montel, J. M., J. Kornprobst, and D. Vielzeuf, Preservation of old U-Th-Pb ages in shielded monazite: Example from the Beni Bousera Hercynian kinzigites (Morocco), *J. Metamorph. Geol.*, *18*, 335–342, 2000.

Nam, T. N., M. Toriumi, and T. Itaya, P-T-t paths and post-metamorphic exhumation of the Day Nui Con Voi shear zone in Vietnam, *Tectonophysics*, *290*, 299–318, 1998.

Newton, R. C., and H. T. Haselton, Thermodynamics of the garnet-plagioclase-Al2SiO5-quartz geobarometer, in *Thermodynamics of Minerals and Melts*, edited by R. C. Newton, pp.131–147, Springer-Verlag, New York, 1981.

Parrish, R. R., U-Pb dating of monazite and its application to geological problems, *Can. J. Earth Sci.*, *27*, 1431–1450, 1990.

Perchuk, L. L., I. V. Lavrent'eva, Experimental investigation of exchange equilibria in the system cordierite-garnet-biotite, in *Kinetics and Equilibrium in Mineral Reactions*, edited by S. K. Saxena, pp. 199–240, Springer-Verlag, New York, 1984.

Powell, R., and T. J. B. Holland, An internally consistent thermodynamic dataset with uncertainties and correlations, 3, Applications to geobarometry, worked examples and a computer program, *J. Metamorph. Geol.*, *6*, 173–204, 1988.

Pownceby, M. I., and V. J. Wall, Fe-Mn partitioning between garnet and ilmenite: Experimental calibration and applications, *Contrib. Mineral. Petrol.*, *97*, 116–126, 1987.

Press, W. H., B. P. Fannery, S. A. Teukolsky, and W. T. Vetterling, *Numerical Recipes: The Art of Scientific Computing*, 735 pp., Cambridge Univ. Press, New York, 1988.

Reed, S. J. B., Electron probe microanalysis, in *Microprobe Techniques in the Earth Sciences*, edited by P. J. Potts et al., pp. 49–89, Chapman and Hall, New York, 1995.

Robinson, P., The eye of the petrographer, the mind of the petrologist, *Am. Mineral.*, *76*, 1781–1810, 1991.

Roger, F., P. H. Leloup, M. Jolivet, R. Lacassin, P. Trinh, M. Brunel, and D. Seward, Long and complex thermal history of the Song Chay metamorphic dome (northern Vietnam) by multi-system geochronology, *Tectonophysics*, *321*, 449–466, 2000.

Rubatto, D., I. S. Williams, and I. S. Buick, Zircon and monazite response to prograde metamorphism in the Reynolds Range, central Australia, *Contrib. Mineral. Petrol.*, *140*, 458–468, 2001.

Schärer, U., P. Tapponnier, R. Lacassin, P. H. Leloup, Z. Dalai, and J. Shaocheng, Intraplate tectonics in Asia: A precise age for large-scale Miocene movement along the Ailao Shan-Red River shear zone, *China, Earth Planet. Sci. Lett.*, *97*, 65–77, 1990.

Schärer, U., Z. Lian-Sheng, and P. Tapponnier, Duration of strike-slip movements in large shear zones: The Red River belt, *China, Earth Planet. Sci. Lett.*, *126*, 379–397, 1994.

Schuhmacher, M., E. de Cambost, K. D. McKeegan, T. M. Harrison, and H. N. Migeon, In situ U/Pb dating of zircon with the Cameca IMS 1270, in *Secondary Ion Mass Spectrometry, SIMS IX*, edited by A. Benninghoven et al., pp. 919–922, John Wiley, New York, 1994.

Smith, H. A., and B. Barreiro, Monazite U-Pb dating of staurolite grade metamorphism in pelitic schists, *Contrib. Mineral. Petrol.*, *105*, 602–615, 1990.

Smith, H. A., and B. J. Giletti, Lead diffusion in monazite, *Geochim. Cosmochim. Acta*, *61*, 1047–1055, 1997.

Spear, F. S., On the interpretation of peak metamorphic temperatures in light of garnet diffusion during cooling, *J. Metamorph. Geol.*, *9*, 379–388, 1991.

Spear, F. S., *Metamorphic Phase Equilibria and Pressure-Temperature-Time Paths*, 799 pp., Mineral. Soc. of Am., Washington, D. C., 1993.

Spear, F. S., and M. J. Kohn, Program Thermobarometry v1.9, pp. 1–43, Rensselaer Polytech. Inst., Troy, N. Y., 1995.

Stacey, J. S., and J. D. Kramers, Approximation of terrestrial lead isotope evolution by a two-stage model, *Earth Planet. Sci. Lett.*, *26*, 207–221, 1975.

Tapponnier, P., G. Peltzer, A. Y. Le Dain, R. Armijo, and P. Cobbold, Propagating extrusion tectonics in Asia: New insights from simple experiments with plasticine, *Geology*, *10*, 611–616, 1982.

Tapponnier, P., G. Peltzer, A. Y. LeDain, R. Armijo, On the mechanics of the collision between India and Asia, in *Collision Tectonics*, edited by M. P. Coward and A. C. Ries, *Geol. Soc. Spec. Publ.*, *19*, 115–157, 1986.

Townsend, K. L., C. F. Miller, J. L. D'Andrea, J. C. Ayers, T. M. Harrison, and C. D. Coath, Monazite replacement during modification of the Ireteba granite, southern Nevada: Geochronological implications, *Geol. Soc. Am. Abstr. Programs, 30*, *30*, A214, 2000.

Turcotte, D. L., and G. Schubert, *Geodynamics: Applications of Continuum Physics to Geological Problems*, 450 pp., John Wiley, New York, 1982.

Wang, E., and B. C. Burchfiel, Interpretation of Cenozoic tectonics in the right-lateral accommodation zone between the Ailao Shan shear zone and the eastern Himalayan syntaxis, *Int. Geol. Rev.*, *39*, 191–219, 1997.

Wang, J. H., A. Yin, T. M. Harrison, M. Grove, Y. Q. Zhang, and G. H. Xie, A tectonic model for Cenozoic igneous activities in the eastern Indo-Asian collision zone, *Earth Planet. Sci. Lett.*, *188*, 123–133, 2001.

Yin, A., and T. M. Harrison, Geologic evolution of the Himalayan-Tibetan orogen, *Earth Planet. Sci. Lett.*, *28*, 211–280, 2000.

Zhang, L. S., and U. Schärer, Age and origin of magmatism along the Cenozoic Red River shear belt China, *Contrib. Mineral. Petrol.*, *134*, 67–85, 1999.

Zhu, X. F., and R. K. O'Nions, Monazite chemical composition: Some implications for monazite geochronology, *Contrib. Mineral. Petrol.*, *137*, 351–363, 1999.

L. D. Gilley, Department of Geology, University of Kansas, 1475 Jayhawk Blvd., Lawrence, KS 66045, USA. (lstockli@ku.edu)

T. M. Harrison, Research School of Earth Sciences, Australian National University, Canberra, ACT 0200, Australia. (director.rses@anu.edu.au)

P. H. Leloup, CNRS, Institut de Physique du Globe de Paris, 4 Place Jussieu, F-75252 Paris Cedex 05, France. (leloup@ipgp.jussieu.fr)

F. J. Ryerson, Institute of Geophysics and Planetary Physics, Lawrence Livermore National. Laboratory, L 202, P.O. Box 808, Livermore, CA 94550, USA. (ryerson1@llnl.gov)

O. M. Lovera, Department of Earth and Space Sciences, University of California, 405 Hilgard Ave., Los Angeles, CA 90095-1567, USA. (lovera@ucla.edu)

J.-H. Wang, Guangzhou Institute of Geochemistry, Chinese Academy of Sciences, P.O. Box 1131,Wushan, Guangzhou 510640 Guangdong, China.